

Mean-Field Models for Heterogeneous Networks of Two-Dimensional Integrate and Fire Neurons

Wilten Nicola and Sue Ann Campbell

Department of Applied Mathematics, University of Waterloo
Waterloo ON N2L 3G1

November 13, 2021

Abstract

We analytically derive mean-field models for all-to-all coupled networks of heterogeneous, adapting, two-dimensional integrate and fire neurons. The class of models we consider includes the Izhikevich, adaptive exponential, and quartic integrate and fire models. The heterogeneity in the parameters leads to different moment closure assumptions that can be made in the derivation of the mean-field model from the population density equation for the large network. Three different moment closure assumptions lead to three different mean-field systems. These systems can be used for distinct purposes such as bifurcation analysis of the large networks, prediction of steady state firing rate distributions, parameter estimation for actual neurons, and faster exploration of the parameter space. We use the mean-field systems to analyze adaptation induced bursting under realistic sources of heterogeneity in multiple parameters. Our analysis demonstrates that the presence of heterogeneity causes the Hopf bifurcation associated with the emergence of bursting to change from sub-critical to super-critical. This is confirmed with numerical simulations of the full network for biologically reasonable parameter values. This change decreases the plausibility of adaptation being the cause of bursting in hippocampal area CA3, an area with a sizable population of heavily coupled, strongly adapting neurons.

1 Introduction

As computers become more powerful, there is a move to numerically simulate larger and larger model networks of neurons [14]. While simulation is useful for confirming observed behavior it is not as helpful in determining the mechanisms underlying the behavior. The tools of dynamical systems theory, such as bifurcation analysis can be useful in this regard when studying single neuron or small network models. However, they are not viable for large networks, especially if the neurons are not identical. Thus, a common approach is to try to extrapolate large network behavior from detailed analysis of the behavior of individual cells or small networks [26]. This can be problematic as networks can have behavior that is not present in individual cells. For example, individual neurons that are only capable of tonic firing when isolated may burst when coupled in a network [32]. Further, large networks may exhibit behavior not present in smaller networks. For example, Dur-e-Ahmad et al. studied bursting in networks ranging in size from 2 cells to 100. They found that bursting occurred in a larger range of parameters for larger networks [8, Figure 7].

Given the role of bursts in networks of neurons, it is important to understand how a network transitions (bifurcates) from a non-bursting behavior, to bursting. Bursting has been suggested to be a fairly important and information dense firing mode for neurons. For example, single bursts can induce long term potentiation and depression in the hippocampus, which are important processes for learning and memory [24]. Additionally, bursts have been found to carry more information about an animals position in space than isolated spikes alone as place fields have been found to be more accurately defined when considering bursts alone [24]. Additionally, the mechanism we analyze in this paper, adaptation induced bursting has also been suggested as a biologically plausible mechanism for the generation of grid cells via oscillatory interference

of the bursting [33]. However, adaptation induced bursting is a network level phenomenon and we cannot apply bifurcation analysis directly to a network of adapting neurons.

Mean-field theory offers one approach to bridge this gap. In applying this theory, one usually derives (or suggests) a low dimensional system of differential equations that govern the moments of different variables across the network [3]. For example, for a network of all-to-all coupled Izhikevich neurons [13], one can derive a two dimensional system of differential equations for the mean adaptation variable, and the mean synaptic gating variable [19]. Mean-field systems enable one to conduct network level bifurcation analysis and hence to test different hypotheses about large network behavior. For example, Hemond et al. [12] found that when uncoupled, the majority of hippocampal pyramidal neurons in region CA3 do not display bursting. This is contradictory to the observation that burst firing is ubiquitous this region [2, Section 5.3.5]. A possible explanation for these contradictory observations is that bursting is a network level phenomenon. This hypothesis has been tested using bifurcation analysis of the mean-field system derived from a network of Izhikevich neurons [8]. In particular, it was shown that for a network of identical all-to-all coupled neurons fit to experimental data from [12] for CA3 pyramidal cells, bursting occurs for a large range of synaptic conductances and applied currents if the spike frequency adaptation in the neurons is sufficiently strong.

Hemond et al. [12] also observed that the pyramidal neurons in their study were heterogeneous, in particular, the neurons had different degrees of spike frequency adaptation. When the study of [8] was extended to a network of two homogeneous subpopulations of hippocampal neurons with different degrees of spike frequency adaptation, the mean-field equations predict, and numerical simulations confirm, that the region in the parameter space where bursting occurs decreases in size [19]. This would seem to indicate that adaptation induced bursting may not be robust to heterogeneity, however, it is unknown how robust this network level bursting is to heterogeneity in different parameters. An extension of the mean-field system in [19] to large networks of heterogeneous neurons, is needed to fully analyze the robustness of adaptation induced bursting.

The application of mean-field analysis to large networks of heterogeneous neurons has been limited to networks of one dimensional integrate and fire neurons with heterogeneity in the applied current [10, 11, 31]. Hansel and Mato [10, 11] analyze a network of all-to-all coupled quadratic integrate and fire neurons consisting of two subpopulations: one excitatory and one inhibitory. They showed analytically that the tonic firing asynchronous state can lose stability either to a synchronous tonic firing state or a bursting state. Vladimirski et al. [31] analyze a network of all-to-all coupled linear integrate and fire neurons subject to synaptic depression. This model was used to study network induced bursting in the developing chick spinal cord. Their derivation of the mean-field model is based on temporal averaging of the fast synaptic gating variable, in addition to the usual network averaging. This results in a model that only involves the distribution of slow synaptic depression variable and the distribution of firing rates. Vladimirski et al. note that, for their model, increased heterogeneity tends to make population induced bursting more robust. They also note that one cannot understand the behaviour of their network with a single slow, network averaged synaptic depression variable.

The motivation for the present paper is to explore the effect of heterogeneity in parameters on network induced bursting when adaptation is the primary negative feedback acting on the individual firing rates. To this end, we introduce a set of mean-field equations for networks of heterogeneous two-dimensional integrate and fire neurons. While the specific neural model we consider is for neurons with adaptation, our derivation is quite general and could be applied to other integrate and fire models. In contrast with [31] our derivation of the mean-field model does not use temporal averaging thus we end up with a mean-field system which involves the network averaged synaptic gating variables as well as the distribution of adaptation variables. We also allow for heterogeneity in more than one parameter. Our approach is a generalization of that used for homogeneous networks of two dimensional integrate and fire neurons [19], however, in the heterogeneous case it turns out that there are actually multiple mean-field models, as different assumptions can be made during the derivation. This leads us to three distinct mean-field systems, each derived under different assumptions, and used for different purposes. Together, these sets of equations allow us to do bifurcation analysis on large networks, as in the homogeneous case. We show that the bifurcation structure of the heterogeneous network differs both qualitatively and quantitatively from the homogeneous network case. We discuss the

implications of this for network induced bursting in the hippocampus.

When considering a homogeneous network, the mean-field variables are a good approximation for the variables of every neuron. However, this is not the case for a heterogeneous network. If the heterogeneity is large, then the neuron variables may be also widely distributed, rendering information about the first moments less useful. This also implies that the behavior of any individual neuron is less predictable with a mean-field system than it was in the homogeneous case. One of our mean-field systems addresses this problem, giving information about the distributions of the variables instead of just the mean.

When considering a model for a specific heterogeneous network of neurons, one stumbling block is determining the distribution of parameters. Estimates of the distribution can be made through direct intracellular recording of a sufficient number of neurons, and conventional measurements of the biophysical properties (membrane capacitance, voltage threshold, etc.). Unfortunately, this is a very time consuming and intensive process. What is needed is a way of measuring the biophysical parameters of multiple neurons simultaneously. There are a few ways to sample multiple neurons such as multi-unit recordings using tetrode arrays, or two-photon microscopy techniques [4, 9]. However, these techniques typically only tell us about spike times of large (dozens to hundreds of neurons) networks [4]. While an impressive accomplishment, this still does not tell us anything directly about the biophysical properties of the neurons that caused those spikes. In this paper we use a mean-field system to determine an approximate distribution of firing rates for a network given a known distribution of parameters. This is an unusual state of affairs for a mean-field system, as these kinds of systems seldom give information about entire distributions. More importantly however, using a mean-field system, we can invert a distribution of steady state firing rates (which can be obtained from multi-unit recordings) to obtain a distribution of parameters. In fact, this can be done at the individual neuron level, to determine the parameter value for any particular neuron. This allows one to estimate different biophysical parameters, which are difficult to measure at the network level, using easy to measure firing rate distributions. However, the assumptions required for the numerical accuracy of the estimation are fairly strong.

The plan for our article is as follows. Section 1.1 introduces the general class of adapting two-dimensional integrate and fire neurons used in our network models. This class was introduced by Touboul [28], who also completed the bifurcation analysis of the single, uncoupled neuron. Population density methods are briefly introduced in section 1.2, as a population density equation serves as an intermediate step to obtain our mean-field models. Section 2 begins with a review of mean-field theory and the equations for the homogeneous network. This is followed, in sections 2.1-2.3, by the derivation of the three mean-field systems for the heterogeneous network. A comparison of numerical simulations of these mean-field systems and the full network is the subject of section 2.4. Applications of mean-field theory to networks with a single heterogeneous parameter can be found in Section 3 including bifurcation analysis (Section 3.1), distributions of parameters and firing rates (Section 3.2) and using mean-field theory for parameter estimation from firing rate data (Section 3.3). Applications of mean-field theory to networks with multiple sources of heterogeneity are included in section 4. A discussion of our work and its implications can be found in section 5.

2 Materials and Methods

2.1 Nonlinear Integrate and Fire Neurons

We consider a network of two-dimensional integrate and fire models of the form

$$\dot{v} = F(v) - w + I \tag{1}$$

$$\dot{w} = a(bv - w), \tag{2}$$

where v represents the nondimensionalized membrane potential, and w serves as an adaptation variable. Time has also been non-dimensionalized. The dynamical equations (1)-(2) are supplemented by the following discontinuities

$$v(t_{spike}^-) = v_{peak} \Rightarrow \begin{aligned} v(t_{spike}^+) &= v_{reset}, \\ w(t_{spike}^+) &= w(t_{spike}^-) + w_{jump}. \end{aligned} \tag{3}$$

This particular notation was formally introduced by Touboul [28], along with a full bifurcation analysis of this general family of adapting integrate and fire neurons. Members of this family include the Izhikevich model [13], the adaptive exponential (AdEx) model [?, 18], and Touboul's own quartic model [28].

The methods of this paper can be applied to a network of any particular neuron belonging to this general family, and thus all derivations are done for this model. For the numerical examples, however, we only consider the Izhikevich neuron:

$$C\dot{V}_i = k(V_i - V_T)(V - V_R) - W_i + I_{app,i} \quad (4)$$

$$\dot{W}_i = \frac{\eta(V_i - V_R) - W_i}{\tau_W} \quad (5)$$

$$V_i(t_{spike}^-) = V_{peak} \Rightarrow \begin{aligned} V_i(t_{spike}^+) &= V_{reset} \\ W_i(t_{spike}^+) &= W_i(t_{spike}^-) + W_{jump,i}, \end{aligned} \quad (6)$$

In dimensionless form, this is given by (1)-(3) with $F(v) = v(v - \alpha)$ in addition to dimensionless versions of the discontinuities (6). The application to other neural models is straight forward, see [19] where the homogeneous mean-field theory has been derived and tested for both the AdEx and the Izhikevich models.

Networks of these neurons can be coupled together through changes in the synaptic conductance. The synaptic conductance of post-synaptic neuron i due to presynaptic neurons $j = 1, 2, \dots, N$ is given by

$$g_i(t) = g_i s_i(t) = \frac{g_i}{N} \sum_{j=1}^N s_{ij}(t), \quad (7)$$

where g_i denotes the maximal synaptic conductance of neuron i and $s_i(t)$ denotes the total proportion of postsynaptic ion channels open in the membrane of neuron i . The time dependent variable $s_{ij}(t)$ represents the proportion of postsynaptic ion channels open in the membrane of neuron i as a result of the firing in neuron j .

The changes in $s_{ij}(t)$ that occur after a spike are often modeled as transient pulses. For example, if neuron j fires its k th action potential at time $t = t_{j,k}$, then the variable $s_{ij}(t)$ at time t is given by

$$s_{ij}(t) = \sum_{t_{j,k} < t} E(t - t_{j,k}). \quad (8)$$

There are different functions proposed for $E(t)$ in the literature including the simple exponential, the alpha synapse, and the double exponential. We primarily consider the simple exponential synapse

$$E(t) = s_{jump} \exp\left(\frac{-t}{\tau_s}\right), \quad (9)$$

which is governed by the ordinary differential equation

$$\frac{ds_{ij}(t)}{dt} = -\frac{s_{ij}}{\tau_s} + s_{jump} \sum_{t_{j,k} < t} \delta(t - t_{j,k}). \quad (10)$$

In the rest of the paper, we assume all-to-all connectivity and that the synaptic parameters s_{jump} , and τ_s are the same for every synapse. In this case we may set $s_i(t) = s(t)$ for all i , as each postsynaptic neuron receives the same summed input from all the presynaptic neurons. Then, using (7) and (10), the network of all-to-all coupled neurons that we consider is given by the following system of discontinuous ODE's:

$$\dot{v}_i = F(v_i) - w_i + I_i + g_i s(t)(E_r - v_i), \quad (11)$$

$$\dot{w}_i = a_i(bv_i - w_i), \quad (12)$$

$$\dot{s} = -\frac{s}{\tau_s} + \frac{s_{jump}}{N} \sum_{j=1}^N \sum_{t_{j,k} < t} \delta(t - t_{j,k}), \quad (13)$$

$$(14)$$

$$v_i(t_{j,k}^-) = v_{peak} \quad \Rightarrow \quad \begin{aligned} v_i(t_{j,k}^+) &= v_{reset}, \\ w_i(t_{j,k}^+) &= w_i(t_{j,k}^-) + w_{jump}. \end{aligned} \quad (15)$$

for $i = 1, 2, \dots, N$.

In the examples, we consider one or more parameters as the sources of heterogeneity. However, to simplify the notation in the derivations, we use the vector $\boldsymbol{\beta}$ to represent all the heterogeneous parameters. Then, denoting the state variables v and w as the vector \mathbf{x} , we can write the equations for the individual oscillator as

$$\dot{\mathbf{x}} = \mathbf{G}(\mathbf{x}, \boldsymbol{\beta}, s) = \begin{pmatrix} G_1(\mathbf{x}, \boldsymbol{\beta}, s) \\ G_2(\mathbf{x}, \boldsymbol{\beta}) \end{pmatrix} \quad (16)$$

Given a specific heterogeneous parameter, G_1 and G_2 may not depend on $\boldsymbol{\beta}$, or all of the components of $\boldsymbol{\beta}$. However, for the sake of simplicity, we include the dependence in both equations.

Our numerical examples are restricted to the Izhikevich neural model, and we primarily consider the driving current I_i of each neuron, the synaptic conductance g_i and the adaptation jump size, w_{jump} as the source of heterogeneity. However, the mean-field equations we derive can be applied to any of the two-dimensional adapting integrate and fire models, with any heterogeneous parameter or set of parameters.

Finally, we note that in many applications, b is a small parameter, and thus the bv term can be dropped in G_2 . We do this in all our numerical studies. However, one can still derive appropriate mean-field equations if this term is present (see discussion in [19]), and thus we have left the term in the derivations.

2.2 The Population Density Equation

The population density function, $\rho(\mathbf{x}, t)$ determines the density of neurons at a point in phase space, \mathbf{x} , at time t . Consider first the case of a homogeneous network, i.e., all the oscillators have the same parameter values, denoted by $\boldsymbol{\beta}$. In the limit as $N \rightarrow \infty$, one can derive the following evolution equation for the population density function:

$$\frac{\partial \rho(\mathbf{x}, t)}{\partial t} = -\nabla \cdot \mathbf{J}(\mathbf{x}, \boldsymbol{\beta}, s, t) \quad (17)$$

where \mathbf{J} is given by

$$\mathbf{J}(\mathbf{x}, \boldsymbol{\beta}, s, t) = \mathbf{G}(\mathbf{x}, \boldsymbol{\beta}, s)\rho(\mathbf{x}, t) = (J^V, J^W). \quad (18)$$

and must satisfy the boundary condition

$$J^V(v_{peak}, w, \boldsymbol{\beta}, s, t) = J^V(v_{reset}, w + w_{jump}, \boldsymbol{\beta}, s, t). \quad (19)$$

In the same limit, the differential equation for s converges to

$$s' = -\frac{s}{\tau_s} + s_{jump} \int_W J^V(v_{peak}, w, s, \boldsymbol{\beta}, t) dw \quad (20)$$

where the integral term is actually the network averaged firing rate, which we denote as $\langle R(t) \rangle$. Derivations of equation (17) can be found in various sources [20, 21].

Equation (17) is frequently referred to as the continuity equation and it has various applications besides its use as an intermediate step in mean-field reductions. For example, the equation has been used to determine the stability of the asynchronous tonic firing state by various authors [1, 11, 25, 27, 29, 30]. These papers predominantly consider homogeneous networks of linear integrate and fire neurons. The exception is the work of Hansel and Mato [11] which considers heterogeneity in the applied current. One can study stability of various firing states using spectral analysis or other analytical treatments of this equation [1, 11, 15, 23, 25, 27, 29]. However, these approaches are too complicated for the models we consider in this paper.

Now consider a heterogeneous network where the parameters vary from oscillator to oscillator, but are static in time. Then one can rewrite the equations for the individual oscillator as

$$\dot{v}_i = G_1(\mathbf{x}_i, \boldsymbol{\beta}_i, s), \quad (21)$$

$$\dot{w}_i = G_2(\mathbf{x}_i, \boldsymbol{\beta}_i), \quad (22)$$

$$\dot{\boldsymbol{\beta}}_i = 0. \quad (23)$$

In this case the flux contribution due to $\boldsymbol{\beta}$ is 0, and the evolution equation for the network is given by

$$\frac{\partial \rho(\mathbf{x}, \boldsymbol{\beta}, t)}{\partial t} = -\nabla \cdot \mathbf{J}(\mathbf{x}, \boldsymbol{\beta}, s, t) \quad (24)$$

The density now has the vector of parameters, $\boldsymbol{\beta}$, as an independent variable. The flux consists of the vector $(J^V, J^W, 0)$, with $\boldsymbol{\beta}$ as an independent variable, as opposed to a fixed constant. If the parameters are time varying however, the final component of the flux will be non-zero. The equation for s is also different in the heterogeneous case:

$$s' = -\frac{s}{\tau_s} + s_{jump} \int_W \int_{\boldsymbol{\beta}} J^V(v_{peak}, w, s, \boldsymbol{\beta}', t) dw d\boldsymbol{\beta}'. \quad (25)$$

While the evolution equation (24) is an exact representation for the network in the large network limit, it is difficult to work with analytically. Additionally, as the dimensions of the PDE become large, it becomes difficult to find numerical solutions efficiently [16]. However, mean-field reductions of the network can be used to reduce the population density PDE to a system of nonlinear switching ODEs that governs the moments of the distribution. Unlike the PDE, the system of ODEs is tractable using bifurcation theory, at least numerically. Furthermore, we show that in the heterogeneous case, the resulting mean-field systems can yield more information than just the type of bifurcation that the network can undergo.

2.3 Mean-Field Theory

In the homogeneous case, the mean-field system of equations for an all-to-all coupled Izhikevich network was derived in [19]. We present here a quick summary of this derivation. In order to derive a mean-field system of equations, one first needs to reduce the PDE for $\rho(\mathbf{x}, \mathbf{t}) = \rho(\mathbf{v}, \mathbf{w}, \mathbf{t})$ by a dimension. This is done by first writing the density in its conditional form:

$$\rho(v, w, t) = \rho_V(v, t) \rho_W(w|v, t) \quad (26)$$

and then integrating the continuity equation with respect to w . This yields the one dimensional PDE

$$\frac{\partial \rho_V(v, t)}{\partial t} = -\frac{\partial G_1(v, s, \langle w|v \rangle) \rho_V(v, t)}{\partial v} = -\frac{\partial J(v, \langle w|v \rangle, s, t)}{\partial v}, \quad (27)$$

where the flux has been redefined to

$$J(v, \langle w|v \rangle, s, t) = \int_W J^V(v, w, s, t) dw. \quad (28)$$

One can now make a first order moment closure assumption, $\langle w|v \rangle = \langle w \rangle$, and derive an approximate ODE for $\langle w \rangle$, which yields the system

$$\begin{aligned} \frac{\partial}{\partial t} \rho(v, t) &= -\frac{\partial}{\partial v} ((F(v) - \langle w \rangle) + I + g(E_r - v)s) (\rho(v, t)) \\ \langle w \rangle' &= \frac{b\langle v \rangle - \langle w \rangle}{\tau_w} + w_{jump} J(v_{peak}, \langle w \rangle, s, t) \\ s' &= -\frac{s}{\tau_s} + s_{jump} J(v_{peak}, \langle w \rangle, s, t) \end{aligned}$$

where the subscript on the density function has been dropped for convenience. The details, and validity of the first order moment closure assumption that is used can be found in [16]. We note however that the work in [16] was primarily with leaky integrate and fire neurons, as opposed to the two-dimensional adapting class we consider here. However, it is a necessary assumption to proceed analytically. If we assume that the adaptation time constant, $\tau_w = \frac{1}{a}$ is large, one can apply a quasi-steady state approximation to derive a system of switching ODE's for $\langle w \rangle$ and s :

$$\langle w \rangle' = \frac{b\langle v \rangle - \langle w \rangle}{\tau_w} + w_{jump} \langle R_i(t) \rangle \quad (29)$$

$$s' = -\frac{s}{\tau_s} + s_{jump} \langle R_i(t) \rangle \quad (30)$$

$$\langle R_i(t) \rangle = \begin{cases} \left[\int_V \frac{dv}{F(v) - \langle w \rangle + I + g(e_r - v)s} \right]^{-1} & : H(\langle w \rangle, s) \geq 0 \\ 0 & : H(\langle w \rangle, s) < 0 \end{cases} \quad (31)$$

The switching manifold for the system, $H(\langle w \rangle, s)$ is given by:

$$H(\langle w \rangle, s) = I - \langle w \rangle + \min_v (F(v) + g(e_r - v)s). \quad (32)$$

Note that $H(\langle w \rangle, s)$ depends on the parameter(s) of the model, and thus for the heterogeneous case, we make this dependence explicit by writing $H(\langle w \rangle, s, \beta)$. As the computation for $\langle v \rangle$ is somewhat lengthy and is only outlined in the discussion of [19], we have placed it in Appendix A.

For the Izhikevich neuron, equations (31)-(32) become

$$\langle R_i(t) \rangle = \begin{cases} \left[\int_V \frac{dv}{v(v-\alpha) - \langle w \rangle + I + g(e_r - v)s} \right]^{-1} & : H(\langle w \rangle, s) \geq 0 \\ 0 & : H(\langle w \rangle, s) < 0 \end{cases} \quad (33)$$

$$H(\langle w \rangle, s) = I - \langle w \rangle - \frac{(\alpha + gs)^2}{4} + ge_r s. \quad (34)$$

Note that in this case, we can evaluate $\langle R_i(t) \rangle$ explicitly:

$$\langle R_i(t) \rangle = \begin{cases} \frac{\sqrt{I - I^*(\langle w \rangle)}}{\arctan\left(\frac{v_{peak} - \frac{\alpha + gs}{2}}{\sqrt{I - I^*(\langle w \rangle, s)}}\right) - \arctan\left(\frac{v_{reset} - \frac{\alpha + gs}{2}}{\sqrt{I - I^*(\langle w \rangle, s)}}\right)} & : H(\langle w \rangle, s) \geq 0 \\ 0 & : H(\langle w \rangle, s) < 0 \end{cases}$$

in addition to an approximation to $\langle v \rangle$

$$\langle v \rangle = \begin{cases} \frac{\langle R_i(t) \rangle}{2} \log\left(\frac{(v_{peak} - \frac{\alpha + gs}{2})^2 + H(\langle w \rangle, s)}{(v_{reset} - \frac{\alpha + gs}{2})^2 + H(\langle w \rangle, s)}\right) + \frac{\alpha + gs}{2} & : H(\langle w \rangle, s) \geq 0 \\ \frac{\alpha + gs}{2} - \sqrt{-H(\langle w \rangle, s)} & : H(\langle w \rangle, s) < 0 \end{cases} \quad (35)$$

A comparison of solutions of these equations and the full network are shown in Figure 1 for both the tonic firing and the bursting case.

This system of equations is valid when $\tau_w \gg O(1)$, however the magnitude of τ_s is also significant. While in the original derivation of [19], $\tau_s = O(\tau_w)$ was suggested as a criterion for validity, this is not actually necessary. One merely requires that τ_s not be significantly smaller than $O(1)$, the time scale of the PDE. The reason for this is that if the time scale of the ODE for s is smaller than that of the PDE then the quasi-steady state approximation must be applied to the ODE for s as well. The requirements on the time constants are carried forward in the heterogeneous case.

In our models, the timescale of the ODE for s is typically between that of the PDE and that of the ODE for w , and we have not applied the quasi-steady approximation to s . Applying a quasi-steady state approximation to both s and the reduced PDE yields a more compact system, which is just an ODE for $\langle w \rangle$, however the analysis does not get any simpler. The reason for this is two-fold: the ODE for $\langle w \rangle$ remains

non-smooth, and the firing rate now has to be implicitly solved at each time step. Thus, it is more convenient to apply the quasi-steady state approximation only to the partial differential equation.

When parameter heterogeneity is added into the mix, it turns out that there are multiple “mean-field” systems of equations that can be derived, by applying different assumptions on the conditional moments. We outline three different assumptions that can be made, and the resulting system of mean-field equations in each case.

2.3.1 Mean-Field System I

We begin by writing out the density function in the conditional form

$$\rho(\mathbf{x}, \boldsymbol{\beta}, t) = \rho_{\mathbf{x}}(\mathbf{x}, t) \rho_{\boldsymbol{\beta}}(\boldsymbol{\beta} | \mathbf{x}, t) \quad (36)$$

The continuity equation is then given by

$$\frac{\partial (\rho_{\mathbf{x}}(\mathbf{x}, t) \rho_{\boldsymbol{\beta}}(\boldsymbol{\beta} | \mathbf{x}, t))}{\partial t} = -\nabla \cdot \mathbf{J}(\mathbf{x}, s, \boldsymbol{\beta}, t). \quad (37)$$

Simple integration with respect to $\boldsymbol{\beta}$ yields the reduced continuity equation

$$\frac{\partial \rho_{\mathbf{x}}(\mathbf{x}, t)}{\partial t} = -\nabla \cdot \mathbf{J}(\mathbf{x}, s, \langle \boldsymbol{\beta} | \mathbf{x} \rangle, t). \quad (38)$$

This step is valid for all the non-dimensionalized models we consider as they are all linear in their dimensionless parameters (see [28]). The flux has also been redefined upon integration to

$$(J^V, J^W) = \rho_{\mathbf{x}}(\mathbf{x}, t) (G_1(\mathbf{x}, \langle \boldsymbol{\beta} | \mathbf{x} \rangle, s), G_2(\mathbf{x}, \langle \boldsymbol{\beta} | \mathbf{x} \rangle)).$$

We now apply the moment closure assumption $\langle \boldsymbol{\beta} | \mathbf{x} \rangle = \langle \boldsymbol{\beta} \rangle$ to yield the following PDE:

$$\frac{\partial \rho_{\mathbf{x}}(\mathbf{x}, t)}{\partial t} = -\nabla \cdot \mathbf{J}(\mathbf{x}, s, \langle \boldsymbol{\beta} \rangle, t). \quad (39)$$

It should be clear that this is equivalent to the continuity equation for a homogeneous network with parameter values fixed at $\langle \boldsymbol{\beta} \rangle$. Thus, the associated mean-field system is identical to the homogeneous case, only with the parameters fixed at $\langle \boldsymbol{\beta} \rangle$. This is the simplest assumption one can make in the heterogeneous case. For example, if we treat I as the source of heterogeneity for a network of Izhikevich neurons, with distribution $\rho_I(I)$, then the resulting mean-field system is

$$\langle w \rangle' = \frac{b \langle v \rangle - \langle w \rangle}{\tau_w} + w_{jump} \langle R_i(t) \rangle \quad (40)$$

$$s' = -\frac{s}{\tau_s} + s_{jump} \langle R_i(t) \rangle \quad (41)$$

$$\langle R_i(t) \rangle = \begin{cases} \left(\int_V \frac{dv}{v(v-\alpha) - \langle w \rangle + \langle I \rangle + g(e_r - v)s} \right)^{-1} & : H(\langle w \rangle, s, \langle I \rangle) \geq 0 \\ 0 & : H(\langle w \rangle, s, \langle I \rangle) < 0 \end{cases} \quad (42)$$

$$H(\langle w \rangle, s, \langle I \rangle) = \langle I \rangle - \langle w \rangle - \frac{(\alpha + gs)^2}{4} + ge_r s \quad (43)$$

$$\langle v \rangle = \begin{cases} \frac{\langle R_i(t) \rangle}{2} \log \left(\frac{(v_{peak} - \frac{\alpha + gs}{2})^2 + H(\langle w \rangle, s, \langle I \rangle)}{(v_{reset} - \frac{\alpha + gs}{2})^2 + H(\langle w \rangle, s, \langle I \rangle)} \right) + \frac{\alpha + gs}{2} & : H(\langle w \rangle, s, \langle I \rangle) \geq 0 \\ \frac{\alpha + gs}{2} - \sqrt{-H(\langle w \rangle, s, \langle I \rangle)} & : H(\langle w \rangle, s, \langle I \rangle) < 0 \end{cases} \quad (44)$$

Note that I in equations (33)-(34) has been replaced by $\langle I \rangle$ in equations (42)-(44). We treat this system as the baseline mean-field model for comparison purposes, in addition to direct numerical simulations of the network, and we denote this system of equations as mean-field one (MFI). We should expect this system to

be an adequate approximation to the actual network for narrowly centered distributions of the parameter heterogeneity (small values of the variance, σ_β).

This set of differential equations is representative of a common approach taken when fitting actual neurons. In this approach, multiple estimates of parameters or measurements taken from multiple neurons are averaged to yield a single parameter value, which is really the mean parameter value, $\langle \beta \rangle$. Simulations of homogeneous, large networks are then run with the parameters fixed at their mean values. As we shall see in subsequent sections, the behavior of a simulated heterogeneous network can differ substantially from that of MFI.

2.3.2 Mean-Field System II

To derive our second mean-field system, we begin by writing the density function in the alternative conditional form

$$\rho(v, w, \beta, t) = \rho_W(w, t | \beta, v) \rho_V(v, t | \beta) \rho_\beta(\beta). \quad (45)$$

Next we integrate the continuity equation with respect to w . This yields the following system

$$\begin{aligned} \frac{\partial \rho_V(v, t | \beta)}{\partial t} \rho_\beta(\beta) &= - \int_W \left(\frac{\partial J^V(v, w, s, \beta, t)}{\partial v} + \frac{\partial J^W(v, w, s, \beta, t)}{\partial w} \right) dw \\ &= - \frac{\partial}{\partial v} J(v, \langle w | v, \beta \rangle, s, \beta, t) - J^W(v, w, s, \beta, t) |_{\partial W} \\ &= - \frac{\partial}{\partial v} J(v, \langle w | v, \beta \rangle, s, \beta, t), \end{aligned} \quad (46)$$

where the last term vanishes as J^W is assumed to be vanishing on the boundary, and

$$J(v, \langle w | v, \beta \rangle, s, \beta, t) = \int_W J^W(v, w, s, \beta, t) dw. \quad (47)$$

We now make the first order moment closure assumption $\langle w | v, \beta \rangle = \langle w \rangle$. Then to complete the system, we must derive a differential equation for $\langle w \rangle$:

$$\begin{aligned} \langle w \rangle' &= \int_V \int_W \int_\beta w \frac{\partial \rho(v, w, \beta, t)}{\partial t} d\beta dw dv \\ &= - \int_V \int_W \int_\beta w \left(\frac{\partial J^W}{\partial w} + \frac{\partial J^V}{\partial v} \right) d\beta dw dv \\ &= \int_V \int_W \int_\beta G_2(v, w, \beta) \rho(v, w, \beta, t) d\beta dw dv \\ &\quad - \int_W \int_\beta w (J^V(v_{peak}, w, s, \beta, t) - J^V(v_{reset}, w, s, \beta, t)) d\beta dw \\ &= \langle G_2(v, w, \beta) \rangle - \int_W \int_\beta w (J^V(v_{peak}, w, s, \beta, t) - J^V(v_{peak}, w - w_{jump}, s, \beta, t)) d\beta dw \quad (48) \\ &= \langle G_2(v, w, \beta) \rangle + \int_\beta \int_W w_{jump} J^V(v_{peak}, w, s, \beta, t) dw d\beta + O(w_{jump}^2) \\ &\approx G_2(\langle v \rangle, \langle w \rangle, \langle \beta \rangle) + \int_\beta w_{jump} J(v_{peak}, \langle w \rangle, s, \beta, t) d\beta. \end{aligned} \quad (49)$$

Note that we have made the approximation $\langle G_2(v, w, \beta) \rangle = G_2(\langle v \rangle, \langle w \rangle, \langle \beta \rangle)$ in addition to dropping the $O(w_{jump}^2)$ terms. Additionally, the substitution on line (48) comes from the boundary condition (19).

Applying a quasi-steady state approximation to the PDE (46) yields the following equation for the steady state voltage independent flux, $J(s, \langle w \rangle, \boldsymbol{\beta})$:

$$J(s, \langle w \rangle, \boldsymbol{\beta}) = \begin{cases} \left[\int_V \frac{dv}{G_1(v, s, \langle w \rangle, \boldsymbol{\beta})} \right]^{-1} \rho_\beta(\boldsymbol{\beta}) & \text{if } H(\langle w \rangle, s, \boldsymbol{\beta}) \geq 0 \\ 0 & \text{if } H(\langle w \rangle, s, \boldsymbol{\beta}) < 0 \end{cases}. \quad (50)$$

We interpret the ratio $J(s, \langle w \rangle, \boldsymbol{\beta})/\rho_\beta(\boldsymbol{\beta})$ as the parameter dependent (or conditional) network averaged firing rate, $\langle R_i(t) | \boldsymbol{\beta} \rangle$, based on the fact that

$$\int_{\boldsymbol{\beta}} J(s, \langle w \rangle, \boldsymbol{\beta}) d\boldsymbol{\beta} \approx \langle R_i(t) \rangle.$$

In other words, the distribution of parameters induces a distribution of firing rates across the network, and the network averaged firing rate is the mean of the distribution.

In summary, the resulting mean-field equations are given by:

$$\langle w \rangle' = \frac{b\langle v \rangle - \langle w \rangle}{\tau_w} + \int_{\boldsymbol{\beta}} w_{jump} \langle R_i(t) | \boldsymbol{\beta} \rangle \rho_\beta(\boldsymbol{\beta}) d\boldsymbol{\beta} \quad (51)$$

$$s' = -\frac{s}{\tau_s} + s_{jump} \int_{\boldsymbol{\beta}} \langle R_i(t) | \boldsymbol{\beta} \rangle \rho_\beta(\boldsymbol{\beta}) d\boldsymbol{\beta} \quad (52)$$

$$\langle R_i(t) | \boldsymbol{\beta} \rangle = \begin{cases} \left[\int_V \frac{dv}{G_1(v, s, \langle w \rangle, \boldsymbol{\beta})} \right]^{-1} & : H(\langle w \rangle, s, \boldsymbol{\beta}) \geq 0 \\ 0 & : H(\langle w \rangle, s, \boldsymbol{\beta}) < 0 \end{cases} \quad (53)$$

$$H(\langle w \rangle, s, \boldsymbol{\beta}) = I - \langle w \rangle + \min_v (F(v) + g(e_r - v)s) \quad (54)$$

$$\langle v \rangle = \int_{\boldsymbol{\beta}} \langle v | \boldsymbol{\beta} \rangle \rho_\beta(\boldsymbol{\beta}) d\boldsymbol{\beta} \quad (55)$$

where the forms of $G_1(v, s, \langle w \rangle, \boldsymbol{\beta})$ and $H(\langle w \rangle, s, \boldsymbol{\beta})$ depend on which specific neural model is used, and the equation for $\langle v | \boldsymbol{\beta} \rangle$ can be found in Appendix A. Note that the distribution of firing rates is not computed explicitly in these equations, only the conditional firing rates, $\langle R_i(t) | \boldsymbol{\beta} \rangle$, are computed. However, we show in section 3.2.2 that a distribution for the steady state firing rates of the network can be computed using $\langle R_i(t) | \boldsymbol{\beta} \rangle$.

We refer to equations (51)-(55) as mean-field two (MFII). It should be noted that MFI and MFII effectively differ in the order in which the integrations are carried out. In MFI, we integrate with respect to $\boldsymbol{\beta}$ first, and then apply the first order moment closure assumptions $\langle \boldsymbol{\beta} | \boldsymbol{x} \rangle = \langle \boldsymbol{\beta} \rangle$ and $\langle w | v \rangle = \langle w \rangle$. In MFII, we integrate with respect to w first, and then apply the moment closure assumption $\langle w | v, \boldsymbol{\beta} \rangle = \langle w \rangle$. Furthermore, if $\langle R_i(t) | \boldsymbol{\beta} \rangle$ does not actually depend on the heterogeneous parameter $\boldsymbol{\beta}$, such as when the heterogeneity is in w_{jump} , then MFI and MFII are identical.

In fact the first order moment closure assumption used here can be weakened. This leads to the ‘‘mean-field’’ system in the next subsection, which is a different kind of system than MFI and MFII.

2.3.3 Mean-Field System III

Suppose that instead of assuming that $\langle w | v, \boldsymbol{\beta} \rangle = \langle w \rangle$, we make the weaker assumption that $\langle w | v, \boldsymbol{\beta} \rangle = \langle w | \boldsymbol{\beta} \rangle$. It turns out that this assumption yields a PDE, even when one makes the quasi-steady state approximation, as we now show. Applying this weaker moment closure assumption to (46) yields the following simplification of the continuity equation:

$$\frac{\partial \rho_V(v, t | \boldsymbol{\beta})}{\partial t} \rho_\beta(\boldsymbol{\beta}) = -\frac{\partial}{\partial v} J(v, \langle w | \boldsymbol{\beta} \rangle, s, \boldsymbol{\beta}, t). \quad (56)$$

Application of the quasi-steady state approximation now yields

$$\begin{aligned}
J(v, s, \langle w|\boldsymbol{\beta} \rangle, \boldsymbol{\beta}) &= \begin{cases} \left[\int_V \frac{dv}{G_1(v, s, \langle w|\boldsymbol{\beta} \rangle, \boldsymbol{\beta})} \right]^{-1} \rho_{\boldsymbol{\beta}}(\boldsymbol{\beta}) & : H(\langle w|\boldsymbol{\beta} \rangle, s, \boldsymbol{\beta}) \geq 0 \\ 0 & : H(\langle w|\boldsymbol{\beta} \rangle, s, \boldsymbol{\beta}) < 0 \end{cases}, \\
H(\langle w|\boldsymbol{\beta} \rangle, s, \boldsymbol{\beta}) &= I - \langle w|\boldsymbol{\beta} \rangle + \min_v (F(v) + g(e_r - v)s).
\end{aligned}$$

An equation for the time variation of $\langle w|\boldsymbol{\beta} \rangle$ can be derived in a similar manner to the last section, yielding the following mean-field system:

$$\langle w|\boldsymbol{\beta} \rangle' = \frac{b\langle v|\boldsymbol{\beta} \rangle - \langle w|\boldsymbol{\beta} \rangle}{\tau_w} + w_{jump} \langle R_i(t)|\boldsymbol{\beta} \rangle \quad (57)$$

$$s' = -\frac{s}{\tau_s} + s_{jump} \int_{\boldsymbol{\beta}} \langle R_i(t)|\boldsymbol{\beta} \rangle \rho_{\boldsymbol{\beta}}(\boldsymbol{\beta}) d\boldsymbol{\beta} \quad (58)$$

$$\langle R_i(t)|\boldsymbol{\beta} \rangle = \begin{cases} \left[\int_V \frac{dv}{G_1(v, s, \langle w|\boldsymbol{\beta} \rangle, \boldsymbol{\beta})} \right]^{-1} & : H(\langle w|\boldsymbol{\beta} \rangle, s, \boldsymbol{\beta}) \geq 0 \\ 0 & : H(\langle w|\boldsymbol{\beta} \rangle, s, \boldsymbol{\beta}) < 0 \end{cases} \quad (59)$$

Note that $\langle w \rangle$ can be computed via:

$$\langle w \rangle = \int_{\boldsymbol{\beta}} \langle w|\boldsymbol{\beta} \rangle \rho_{\boldsymbol{\beta}}(\boldsymbol{\beta}) d\boldsymbol{\beta}. \quad (60)$$

We denote this system as mean-field three (MFIII). Note that the equation for $\langle w|\boldsymbol{\beta} \rangle$ is actually a PDE. Thus, while this system should be more accurate than mean-field II, it has the drawback of being more difficult to analyze. The dependence on $\boldsymbol{\beta}$ forces one to discretize over a mesh in $\boldsymbol{\beta}$ in order to work numerically with this system. This makes numerical bifurcation analysis more difficult. However, as we shall show later, an approach that yields similar information to direct bifurcation analysis can be used with MFIII. The equation for $\langle v|\boldsymbol{\beta} \rangle$ can once again be found in the appendix.

3 Results

3.1 Numerical Simulations

Recall that simulations of a homogeneous network and the corresponding mean-field system are shown in Figure 1. Note that the network undergoes a bifurcation from tonically firing to bursting as the amount of applied current I_{app} is decreased, with all other parameter values held fixed. Further simulations show that if I_{app} is decreased below I_{rh} then all neurons in the network are quiescent (non-firing).

To determine and compare the validity of the three mean-field systems, we have run a series of numerical simulations of these systems and of an actual network containing 1000 neurons. The parameter values for the individual neurons can be found in Table 1. They are based on those given in [8] which were fit to data for hippocampal CA3 pyramidal neurons from [12]. These are the parameter values we use for the rest of this paper, unless otherwise indicated.

To begin, we consider heterogeneity only in the applied current. The distributions are assumed to be normal with mean $\langle I \rangle$ and standard deviation σ_I . We varied the values of the mean and standard deviation and found that the accuracy of the mean-field approximations depends on where the mean is relative to the different bifurcation regions and on the size of the standard deviation.

As for the homogeneous network, the heterogeneous network undergoes a bifurcation from tonic firing to bursting as the amount of current applied to the individual neurons is decreased, with all other parameters held fixed. This can be seen in Figure 2 where the bifurcation with decreasing $\langle I_{app} \rangle$ is shown. As $\langle I_{app} \rangle$ is decreased below I_{rh} , there is a bifurcation to quiescence. We will not discuss this latter bifurcation in detail, as we are primarily interested in analyzing the transition from tonic firing to bursting.

Note that the bifurcations described above only occur in the mean sense. Since the current values are normally distributed, there is non-zero probability that some neurons receive large enough or small enough

current to be in a state other than that corresponding to the value of $\langle I_{app} \rangle$. For small enough standard deviations, very few neurons in an actual finite network are likely to have behaviour different from the mean. However, for large standard deviations, a sizable proportion may not follow the mean behaviour.

Given this knowledge of the different qualitative behaviors of the network, we can see how the mean-field systems compare. For tonic firing (Figure 2(a)), even when the standard deviation is large, the mean-field systems approximate the network means $\langle g(t) \rangle$, and $\langle W(t) \rangle$ very well. However, when the network is bursting, with $\langle I_{app} \rangle > I_{rh}$, we see a difference as to which mean-field system is superior. For small values of σ_I , we have numerically found that mean-field I is superior to mean-field II and III, however all the systems are quantitatively and qualitatively accurate (see Figure 2(b),2(c)). However, for larger values of σ_I , the amplitude error of MFIII is the smallest, and MFII is the worst approximation as it bifurcates to tonic firing prematurely.

When $\langle I_{app} \rangle$ is close to I_{rh} , we see even stronger differences between the three mean-field systems. For small to intermediate standard deviations, MFII and MFIII are clearly superior to MFI, having a smaller amplitude and frequency error (see Figure 3(a), 3(b)). However, for larger values of σ_I as shown in Figure 3(c), and 3(d), only MFIII is a qualitatively and quantitatively accurate representation of the behavior of the network. The amplitude and frequency error of MFI are very large, and MFII again bifurcates prematurely to tonic firing.

One should note that for $\langle I_{app} \rangle = O(I_{rh})$ and for large values of σ_I , the network can undergo a period doubling bifurcation. This is shown in Figure 4. The large standard deviation in the current forces different neurons into different regimes, such as tonic firing, bursting, alternate burst firing, and quiescence as seen in Figure 4(b). The fact that a small subpopulation of neurons are alternate bursters (i.e., burst with twice the period of the rest of the bursting neurons) appears as a period doubled limit cycle in the mean variables of the network, as seen in Figure 4(a). Only MFIII is able to approximate the period-doubled limit cycle with any degree of accuracy, as shown in Figure 4(c) and 4(d). Period doubling bifurcations are well known for their capability of inducing chaos. Given that MFIII accurately represents the period doubling bifurcation, it may be able to replicate any potential chaotic behavior. However, we leave further investigation of this interesting behaviour for future work.

To summarize, all the mean-field systems are valid for tonic firing parameter regimes, and MF I is valid for all parameter regimes with small σ_I , except for $\langle I_{app} \rangle = O(I_{rh})$. Mean-Field II and III are valid for bursting with $\langle I_{app} \rangle \gg I_{rh}$, and MFIII is the only valid approximation for $\langle I_{app} \rangle = O(I_{rh})$. Thus, when $\langle I_{app} \rangle$ is large we may be able to use MFII to determine the type of bifurcation(s) involved when a heterogeneous network transitions from tonic firing to bursting and the location in parameter space of the bifurcation manifolds. Note that when the mean network behaviour undergoes a bifurcation from a tonic firing steady state to a bursting oscillation, this does not indicate that the entire network of neurons is bursting, or tonically firing. However, we will show how to use MFIII to determine what proportion of neurons display the different types of behavior, given a specific parameter regime and level of heterogeneity.

In addition to simple heterogeneity using unimodal distributions, one can also apply the same three mean-field equations to networks where multiple subpopulations exist. However, unlike previous attempts at modelling networks with multiple subpopulations, we do not generate discrete coupled subnetworks with different fixed values of the parameters in each subnetwork. Instead we use a smoother approach where the networks have distributions of parameters with multiples modes indicative of multiple subpopulations. This can be easily done through the processing of mixing unimodal distributions (see Appendix C).

3.2 Applications of Mean-Field Theory with a Single Source of Heterogeneity

3.2.1 Bifurcation Types and Manifolds Using MFII

As shown in Fig. 2 the CA3 model network makes transition from tonic firing to bursting as $\langle I_{app} \rangle$ is varied. Similar transitions occur when g_{syn} is varied. In this section, we use numerical bifurcation analysis of MFII to determine the bifurcations involved in this transition, and the manifolds where they occur in the $\langle I_{app} \rangle$ - g_{syn} parameter space. Since the mean-field system (51)–(55) consists of switching ODEs, this involves bifurcations of non-smooth systems as well as standard (smooth) bifurcations. A review of the

theory of non-smooth systems can be found in [7]. The numerical bifurcation analysis is done in MATLAB [17] using the MATCONT package [6] for the standard bifurcations and direct numerical simulations for the non-smooth bifurcations. We compare the mean field theory results to those for the homogeneous system and to direct simulations of large networks.

In [19] we carried out a numerical bifurcation analysis for a homogeneous network. The mean-field equations in this case, which are the same as MFI with $\langle I_{app} \rangle$ replaced by I_{app} , indicate that the transition from tonic firing to bursting occurs via the following sequence of bifurcations. The stable bursting limit cycle is created in a saddle node bifurcation of (nonsmooth) limit cycles. The smaller, unstable limit cycle becomes smooth in a grazing bifurcation and then disappears in a subcritical-Hopf bifurcation which destabilizes the equilibrium point corresponding to tonic firing. This transition is shown in Figure 5(a) when I is held fixed, and g_{syn} is varied. The bursting limit cycles are created at a low g_{syn} value and destroyed at a high g_{syn} value. The sequence of bifurcations is the same in both cases.

Using MFII, we numerically confirm that, as for the homogeneous network, the mean-field system of the heterogeneous network undergoes a Hopf bifurcation as the network transitions from tonic firing to bursting. However, as shown in 5(b), with $\langle I_{app} \rangle$ held fixed the transitions for low g_{syn} and high g_{syn} are not the same. For high g_{syn} the transition is the same as the homogeneous case. For low g_{syn} the transition occurs via the following sequence of bifurcations. A supercritical Hopf bifurcation destabilizes the equilibrium point corresponding to tonic firing and creates a stable limit cycle. This limit cycle is smooth and hence corresponds not to bursting, but to firing with an oscillatory firing rate. This limit cycle then grows until it grazes the switching manifold and becomes a non-smooth, bursting limit cycle in a grazing bifurcation (in Figure 5(b) this occurs at $g_{syn} \approx 150$). We verified this prediction of the mean-field model by running direct simulations of a network of 10,000 neurons with fixed $\langle I_{app} \rangle$, σ_I while varying the g_{syn} value. As shown in Figure 6(a), when the steady state mean variables are plotted vs g_{syn} , the supercritical nature of the Hopf bifurcation in the large network is apparent.

To further investigate the heterogeneous case, we used MATCONT to carry out two parameter continuation of the Hopf bifurcation for MFII with four different values for the standard deviation of I_{app} : $\sigma_I = 250, 500, 750, 1000$ pA. As shown in Figure 6(b), in all cases there appears to be a codimension-2 Bautin (or generalized Hopf) bifurcation on the Hopf manifold, with the Hopf being supercritical on the left boundary before this point and subcritical after. By contrast, in the homogeneous case ($\sigma_I = 0$ line in Figure 6(b)) the bifurcation is subcritical everywhere on the Hopf manifold.

Further verification of the mean-field results can be found in the direct numerical simulations of a network of 500 neurons shown in Figure 6(c). The simulations were run on a 50×50 mesh in the g_{syn} vs $\langle I_{app} \rangle$ parameter space, using five different values for the standard deviation of I_{app} : $\sigma_I = 0, 250, 500, 750, 1000$ pA. Note that $\sigma_I = 0$ is the homogeneous network. The proportion of bursting neurons, p_{burst} , was computed using equation (85) (see Appendix A). The 0% and 100% bursting contours can be seen in 6(c) and 6(d). In these figures, there appear to be two kinds of transitions from tonic firing to bursting. Along the (lower) left part of the boundary of the bursting region, the transition is gradual: the proportion of bursting neurons gradually increases from 0 to 100%. Along the rest of the boundary, however, the whole network transitions to bursting simultaneously. This agrees with the prediction from the mean-field model that two different bifurcations occur along the bursting boundary. Note also that the size of the entire bursting region and the 100% network bursting region get smaller as the level of heterogeneity (σ_I) increases.

Let us reiterate the primary differences between supercritical and subcritical Hopf induced bursting seen in Figures 5 and 6. First, the subcritical case allows for bursting at lower g_{syn} values than the supercritical case. This is because in the subcritical case bursting is initiated via a saddle-node of limit cycles bifurcation which occurs to the *left* of the Hopf bifurcation, while in the supercritical case, bursting starts to the *right* of the Hopf in a grazing bifurcation. Second, the transition to bursting is sharp in the subcritical case and gradual in the supercritical case. The supercritical Hopf bifurcation is consistent with the gradual transition from bursting to firing seen in Figures 6(c) and 6(d). When only a few neurons are bursting and the rest have oscillatory firing rates the corresponding mean behavior is a limit cycle with small amplitude. As more and more neurons become bursting this increases the amplitude of the limit cycle of the mean behavior until it grazes the switching manifold. In the subcritical case, the saddle-node of limit cycles involves large

amplitude limit cycles, corresponding to all the neurons being in the bursting state.

The bifurcation manifolds in Figure 6(b) are both qualitatively and quantitatively accurate descriptions of the behavior of the actual network. For example, in the actual network simulation, the bursting region decreases as σ_I increases (see Figure 6(c)). This same behavior is displayed by the MFII equations, albeit to a greater degree, as shown in Figure 6(b). However, there is a greater degree of quantitative error for lower values of g_{syn} and larger values of σ_I . In particular, for a fixed value of σ_I MFII predicts that the Hopf bifurcation occurs at a higher value of g_{syn} than occurs in the real network (compare Figures 6(b) and 6(c), and 6(d) directly) and this prediction error seems to increase as σ_I increases. This is why MFII indicates the network should be tonically firing when σ_I is high (in Figure 2(d), for example).

Taken together, these results indicate that for small g_{syn} , network induced bursting via adaptation is not robust to heterogeneity in the applied current. This occurs for qualitative and quantitative reasons, both related to the Hopf bifurcation associated with the left boundary of the bursting region. Qualitatively, the addition of heterogeneity causes this bifurcation to change from subcritical to supercritical making the bursting less robust for small g_{syn} values. Quantitatively, the g_{syn} value of this bifurcation increases when the heterogeneity becomes stronger, while the value of the Hopf bifurcation associated with the right boundary does not change appreciably. Thus the size of the bursting region decreases with increasing heterogeneity.

3.2.2 Bifurcation Types and Manifolds Using MFIII

It is difficult to use MATCONT with MFIII as MFIII is an infinite dimensional dynamical system, as it is a PDE. However, the existence of equilibrium points can be determined using standard root finding algorithms. While direct bifurcation analysis is difficult to implement in this situation, one can use properties of the firing rate to describe, qualitatively and quantitatively, any transitions between network states. This will be the approach of this section. To begin, we consider networks that are tonically firing, we then proceed to the study of bursting networks.

For a network of neurons with heterogeneity in the parameters, even if all the neurons are tonically firing, one cannot find a steady state firing rate for the network, as in the case of a homogeneous network. The parameter heterogeneity creates a distribution of steady state firing rates across the network. While the mean-field equations by themselves can only determine the mean of this distribution, with an added assumption we can approximate the distribution of steady state firing rates for the network with a great degree of accuracy.

Consider a network with just one heterogeneous parameter, β . Assume that the steady state firing rate of each neuron in the network can be related to its value for the heterogeneous parameter: $R_i = g(\beta)$. Assume further that one can approximate this function by the steady state value of $\langle R_i(t) | \beta \rangle$:

$$g(\beta) \approx \langle R_i | \beta \rangle. \quad (61)$$

This is easily determined through direct simulation of MFIII, (57)-(59), until the system reaches steady state. Treating g as the transformation of a random variable, one can determine the steady state distribution of firing rates in the network, $\rho_R(r)$, through the standard theorem on transforming random variables:

$$\rho_R(r) = \rho_\beta(g^{-1}(r)) \left| \frac{d}{dr} g^{-1}(r) \right|. \quad (62)$$

which can be found in any standard textbook on probability theory (such as [22]). Note that we must assume that $\langle R_i | \beta \rangle$ is monotonic and invertible for this procedure to be valid.

We carried out this computation for a network of 1000 neurons with a normal distribution in either I , g , or w_{jump} . Details of the implementation can be found in Appendix D We numerically determined the distribution of steady state firing rates for the neurons in the full network through

$$R_i = \frac{1}{ISI_{i,last}}, \quad i = 1, 2, \dots, N \quad (63)$$

where $ISI_{i,last}$ is the last interspike interval for the i^{th} neuron measured from a lengthy (1000 ms) simulation. Figure 7 shows the results of the two approaches. The blue curve in the left column shows the distribution of parameter values. This is used in MFIII to calculate the predicted distribution of firing rates, which is the dashed red curve in the right column. The solid blue curve in the right column is the computed distribution of firing rates from numerical simulation of the full network equations. There is excellent agreement between the firing rate distributions in all cases.

We carried out the same computations with a bi-modal distribution in I , g , or w_{jump} , generated by mixing normal unimodal distributions (see Appendix C). This is one way of representing a network with two subpopulations of neurons with different parameters. The mean field approach again gives an excellent approximation to the qualitative and quantitative properties of the steady state distribution of firing rates, as shown in the right column of Figure 8.

The above approach is only valid when the network is tonically firing. In this situation the steady firing rates of the network and the individual neurons are constant. When the network leaves the tonic firing regime, however, these steady state firing rates become oscillatory. In the case of bursting, the amplitude of the oscillation is large enough that the firing rate goes to zero for intervals of time. Whether or not the neurons are bursting, oscillatory firing rates cannot be represented as a simple distribution of firing rates. However, with some additional work we can use the tools developed above to determine what proportion of neurons in the network is bursting. This is a statistical alternative to direct bifurcation analysis.

From simulations of the full network, we know that when the variance in the heterogeneity is large enough, not all of the neurons necessarily display the behavior predicted from the mean-field equations. For example, Figure 9 shows simulations of a network where the mean-field equations display an oscillatory firing rate which does not quite go to zero. The spike time raster plot of the full network (Figure 9(a)) shows that some neurons *are* bursting while others are tonically firing with an oscillatory firing rate. However, simulation of the corresponding mean-field equations (Figure 9(b), dashed line) reveals only an oscillation, not bursting. While this is consistent with the behaviour of the network mean variables (Figure 9(b), solid line), we have lost the information that some of the neurons are bursting. Similarly, one can find examples where the mean-field equations exhibit bursting, but not all neurons in the network are bursting. Thus, it would be useful to have more information about individual neuron behaviour. MFIII can be used to obtain such information. s.

In the situation described above, the steady state mean network firing rate is oscillatory. We will denote this oscillatory solution as γ . We interpret γ to be the limit cycle parameterized by $\gamma(t)$ with $(s(\gamma(t)), \langle w(\gamma(t)) | \beta \rangle)$ being the graph of the limit cycle in phase space. We will denote the period of the limit cycle as T . In this case, “steady state” firing rate for neuron i will be a periodic function of time: $\bar{R}_i(t)$, which depends on γ and the value of the parameter β associated with the neuron: $\bar{R}_i(t) = g(\beta, \gamma(t))$, for $t \in [0, T]$. To proceed, we make the same assumption as above, that

$$g(\beta, \gamma(t)) \approx \langle R_i(\gamma(t)) | \beta \rangle \quad (64)$$

where $\langle R_i(\gamma(t)) | \beta \rangle$ is the oscillatory firing rate associated with the steady state limit cycle γ in MFIII. An example of the graph of the steady state limit cycle derived from MFIII is shown in Figure 9(c). In this visualization we can clearly see that part of the network is bursting (blue) while the rest is tonically firing with an oscillatory firing rate (green). Integration of this limit cycle over the heterogeneous parameter returns the “mean” limit cycle (Figure 9(d)).

We now use this setup to approximate p_{burst} , the proportion of neurons in the network that are bursting during the network level oscillation γ . Noting that $\langle R_i(\gamma(t)) | \beta \rangle \geq 0$, for all $t \in [0, T]$, the tonically firing neurons correspond to those β values for which $\langle R_i(\gamma(t)) | \beta \rangle > 0$, for all $t \in [0, T]$. Thus we define, p_{tonic} , the proportion of tonically firing neurons in the network via

$$p_{tonic} = \int_{\beta} X \left(\left[\min_{t \in [0, T]} \langle R_i(\gamma(t)) | \beta \rangle \right] > 0 \right) \rho_{\beta}(\beta) d\beta \quad (65)$$

where X is the usual indicator function. Similarly, the proportion of quiescent (nonfiring) neurons is given

by

$$p_q = \int_{\beta} X \left(\left[\max_{t \in [0, T]} \langle R_i(\gamma(t)) | \beta \rangle \right] = 0 \right) \rho_{\beta}(\beta) d\beta. \quad (66)$$

Recall that the bursting neurons correspond to those β values such that $\langle R(\gamma(t)) | \beta \rangle = 0$, for some subinterval of $[0, T]$. Thus we must have

$$p_{burst} = 1 - p_q - p_{tonic}. \quad (67)$$

We compute these values as follows. First we numerically integrated MFIII until the steady state oscillation γ is reached. This is an oscillation of $\langle w(t) | \beta \rangle$, and $s(t)$. The corresponding oscillatory firing rate $\langle R_i(\gamma(t)) | \beta \rangle$ is computed through equation (59) as a function of β on the limit cycle γ . One can then determine

$$m(\beta) = \min_{t \in [0, T]} \langle R(\gamma(t)) | \beta \rangle, \quad (68)$$

$$M(\beta) = \max_{t \in [0, T]} \langle R(\gamma(t)) | \beta \rangle, \quad (69)$$

and the integrals simplify to

$$p_{tonic} = \int_{\beta} H(m(\beta)) \rho_{\beta}(\beta) d\beta \quad (70)$$

$$p_q = \int_{\beta} H(-M(\beta)) \rho_{\beta}(\beta) d\beta \quad (71)$$

where H is the Heaviside function, with $H(0) = 1$.

Numerical results for a network with single heterogeneous parameter are shown in Figure 10. For Figure 10(a), the proportion of bursting neurons was computed, using the method described above, at each point in a mesh on the g_{syn} vs. $\langle I_{app} \rangle$ parameter space. This data was then used to generate the p_{burst} contours. For Figure 10(b) the actual network was simulated to steady state at each point of a slightly coarser mesh. The proportion of bursting neurons at each point was computed according to equation (85) in Appendix B and used to generate the p_{burst} contours. The results of the mean-field computation are both qualitatively and quantitatively accurate. In particular, MFIII recovers the gradual transition to bursting on the left boundary of the bursting region and the abrupt transition to bursting on the right. It should be noted that it is much faster, by approximately an order of magnitude, to run a mesh of integrations over MFIII than it is to run mesh over an actual network.

3.2.3 Inverting a Steady State Firing Distribution to Determine the Distribution of Parameters Using MFIII

Many parameters for neuron models are difficult to measure directly using electrophysiology. However, a distribution of firing rates across a network of neurons is relatively easy to measure using intracellular recordings, or can be estimated using measurements from multi-electrode recordings and spike sorting algorithms, among other methods [4, 9]. We have seen in the previous section that, given a distribution of heterogeneities, MFIII can predict the steady state distribution of firing rates. Here we show that one can invert this process to yield a distribution of parameters given a steady state distribution of firing rates.

We assume that only the firing rate distribution is known, and denote it $\rho_R(r)$ as above. We then proceed as in the previous section, assuming that the steady state firing rate for a particular neuron is some function of the heterogeneous parameters $R_i = g(\beta)$ and that this function is well approximated by $\langle R_i | \beta \rangle$. Under these assumptions, one can solve for the distribution of parameters β using

$$\rho_{\beta}(\beta) = \rho_R(g(\beta)) \left| \frac{d}{d\beta} g(\beta) \right| \quad (72)$$

which follows from standard statistical theorems on the transformations of random variables [22]. Note that we need to assume that $\langle R_i | \beta \rangle$ is differentiable for this procedure to be valid.

The primary problem we face in using this approach to approximate the distribution $\rho_\beta(\beta)$ is that we need to determine the steady state values of the function $\langle R_i|\beta \rangle$. However, a cursory look at the equations for MFIII shows that these in fact depend on $\rho_\beta(\beta)$, the function we are trying to find, through the equation for s :

$$\dot{s} = -\frac{s}{\tau_s} + s_{jump} \int_{\beta} \langle R_i(t)|\beta \rangle \rho_\beta(\beta) d\beta. \quad (73)$$

Fortunately, however, this problem disappears when we look at the steady state value for s :

$$\bar{s} = \tau_s s_{jump} \int_{\beta} \langle R_i|\beta \rangle \rho_\beta(\beta) d\beta = \tau_s s_{jump} \langle R_i \rangle. \quad (74)$$

Here $\langle R_i \rangle$ is the unconditioned steady state mean of the firing rate distribution. This information is readily available, as we have assumed we know the steady state distribution, $\rho_R(r)$, and determining the first moment is numerically trivial.

Putting the expression for \bar{s} into the steady state equation for $\langle w|\beta \rangle$ yields a set of coupled equations:

$$\langle w|\beta \rangle = \tau_w w_{jump} \langle R_i|\beta \rangle, \quad (75)$$

$$\langle R_i|\beta \rangle = \begin{cases} \left[\int_{\mathcal{V}} \frac{dv}{G_1(v, \tau_s s_{jump} \langle R_i \rangle, \langle w|\beta \rangle, \beta)} \right]^{-1} & : H(\langle w|\beta \rangle, \bar{s}, \beta) \geq 0 \\ 0 & H(\langle w|\beta \rangle, \bar{s}, \beta) < 0 \end{cases}. \quad (76)$$

These may be solved for $\langle w|\beta \rangle$ and $\langle R_i|\beta \rangle$ by discretizing in β and numerically solving the resulting system at each grid point with any standard root finding algorithm.

Alternatively, one can set s to its equilibrium value in MFIII and numerically integrate the resulting equation:

$$\langle w|\beta \rangle' = -a \langle w|\beta \rangle + w_{jump} \langle R_i(t)|\beta \rangle, \quad (77)$$

$$\langle R_i(t)|\beta \rangle = \begin{cases} \left[\int_{\mathcal{V}} \frac{dv}{G_1(v, \tau_s s_{jump} \langle R_i \rangle, \langle w|\beta \rangle, \beta)} \right]^{-1} & : H(\langle w|\beta \rangle, s, \beta) \geq 0 \\ 0 & H(\langle w|\beta \rangle, s, \beta) < 0 \end{cases} \quad (78)$$

until it reaches steady state, which will determine $\langle w|\beta \rangle$ and $\langle R_i|\beta \rangle$. Note that this approach will only work if the tonic firing equilibrium of the original mean-field system MFIII is asymptotically stable.

We have implemented this approach as follows. A network of 1000 neurons is numerically integrated until it reaches its steady state firing rate. The distribution of firing rates over the network is found as described in the previous section. The density function for this distribution, $\rho_R(r)$, is then estimated using the firing rate histogram. Equations (77)-(78) are numerically integrated until they reach steady state. We then substitute the estimate of $\rho_R(r)$ and the approximation $\langle R_i|\beta \rangle$ of $g(\beta)$ into (72) to determine the parameter distribution $\rho_\beta(\beta)$. See Appendix D for more details. Our results for unimodal and bimodal distributions are shown in Figure 7 and Figure 8, respectively. In the right column of each figure, the solid blue curve is the distribution of steady state firing rates from integration of the full network. In the left column of each figure the dashed red curve is the estimate of $\rho_\beta(\beta)$ found using the procedure above, while the blue curve is the actual parameter distribution used in the network simulation. We note that no information about the distribution of parameters is known in the estimation procedure, yet the numerical results are very accurate in both the unimodal (Figure 7) and the bi-modal case (Figure 8).

Perhaps most interesting is that we can extend this technique to estimate the individual neuron parameter values, β_i , $i = 1, \dots, N$. This again follows from the assumption that $g(\beta) = \langle R_i|\beta \rangle$ is the function that transforms the random variables β_i into R_i . If the function is invertible, then we can compute the individual β_i through numerically inverting the steady state $\langle R_i|\beta \rangle$. For example, when this technique is applied to a network where the only source of heterogeneity is I , the mean relative absolute error in the predicted values \hat{I}_i versus the actual values I_i is only 0.6%. The details about how to numerically invert for the individual parameter values are included in Appendix D.

While network level inversion of a single heterogeneous parameter is an important step forward, this is performed under very strong assumptions. In particular, when performing this inversion, all of the heterogeneity in the firing rates is assumed to come from a single parameter. Additionally, all the other parameters are assumed to be known. These two assumptions are exceptionally strong and one has to take great care in inverting actual recorded firing rates from neurons that they be reasonably satisfied.

3.3 Mean-Field Applications with Multiple Sources of Heterogeneity

In order for the mean-field applications to be useful for realistic neuronal networks, one needs to consider heterogeneity in more than one parameter. Recall that the mean field systems derived in section 2.3 are valid for multiple heterogeneous parameters, one simply considers β to be a vector instead of scalar. This presents some difficulties in implementation which we discuss in the section. The examples we consider will have 2 or 3 sources of heterogeneity, primarily in the parameters I , g and d .

Recall that MFII is given by the equations (51)-(55). The main difficulty in dealing with MFII lies with the integral terms, which are now multiple integrals. For example:

$$\langle R_i \rangle = \int_{\beta_1} \int_{\beta_2} \dots \int_{\beta_p} \langle R_i | \beta \rangle \rho_{\beta}(\beta_1, \beta_2, \dots, \beta_p) d\beta_p \dots d\beta_2 d\beta_1 \quad (79)$$

where p is the number of heterogeneous parameters. In order to numerically integrate or carry out bifurcation analysis on MFII, these multiple integrals must be evaluated. We have found that this is most easily done using a Monte-Carlo numerical integration scheme. Once this is implemented, bifurcation diagrams can be generated exactly as for the case of one parameter heterogeneity: the equilibrium points and smooth limit cycles are continued using MATCONT, while the nonsmooth limit cycles are generated using numerical simulations.

The integral term in MFIII can be dealt with in a similar way as to that for MFII. Once this is implemented, the steady states and network properties can be determined as described in section 3.2, while numerical simulations can be used to follow stable periodic solutions. We will use this approach later on in our case study on adaptation induced bursting.

Mean-field III can also be used to determine steady state firing rates following the procedure in section 3.2.2, however, one now has to discretize the equations over a multi-dimensional mesh. While this approach is feasible, we found it is more efficient to predict the steady state firing rates of the individual neurons through the following interpolation scheme. Given knowledge of the parameter distribution, we generate sample points β_i from this distribution. We then generate a steady state firing rate for each sample point, $R_i = g(\beta_i)$, where g is determined from MFIII as described in section 3.2.2. We interpolate over the (β_i, R_i) ordered pairs to determine the firing rates of the individual neurons, given knowledge of their parameter values. If we only need the distribution of the firing rates, then the distribution of the R_i is an estimate of this, without need for interpolation. This approach has been applied to a network of 1000 Izhikevich neurons with three simultaneous sources of heterogeneity, as shown in Figure 11.

The one application we found difficult to extend to the case of multiple sources of heterogeneity was the mapping of the distribution of steady state firing rates to the distribution of parameters. There is a fundamental difficulty with this inversion problem: the firing rate distribution is one-dimensional, but the distribution of parameters is multidimensional. Thus, we leave further investigation of this problem for future work.

3.3.1 Bifurcation Analysis With Multiple Sources of Heterogeneity - Case Study

To conclude our work, we consider a realistic model for a CA3 hippocampal network of pyramidal cells. Hemond et al. [12] classify CA3 pyramidal cells into three types: weakly adapting, strongly adapting and intrinsically bursting. We will focus on the effect on network bursting of having two subpopulations: one strongly adapting and one weakly adapting. We use the Izhikevich model (4)-(6) with the parameters set up by [8] (see Table 1), but include heterogeneity in I_{app} , g_{syn} and the adaptation parameters W_{jump} , τ_W . The parameter distributions are generated through distribution mixing (see Appendix B) of normal distributions

with the parameters given in Table 2. We have treated the mean values of I_{app} and g_{syn} from the strongly adapting subpopulation as the bifurcation parameters. We also varied the proportion of strongly adapting neurons in the population, i.e., parameter p in equation (87).

The 0% and 100% bursting contours for simulations over the two parameter mesh in the $\langle I_{app} \rangle, \langle g_{syn} \rangle$ are shown in Figure 12 for both the full network (Figure 12(a)) and MFIII (Figure 12(b)). Numerical bifurcation analysis of MFII (not shown) confirms that the bifurcations are similar to when I_{app} was the only source of heterogeneity, in particular, on the left boundary of the bursting region the Hopf bifurcation is supercritical, while on the right it is subcritical.

As shown in Figure 12, when the proportion of strongly adapting neurons is decreased, the bursting region decreases. However, unlike previous results [19, Figure 10], the decrease seems to be more pronounced in the high g_{syn} region. This is likely due to having truly heterogeneous distributions of parameters, as opposed to splitting a network into two different homogeneous subpopulations as was done in [19]. In all cases, it appears that heterogeneity shifts the bursting manifold outside of the low g_{syn} region, which we suggest is the region of biologically plausible conductances [19].

4 Discussion

Building on the mean-field framework for networks of homogeneous oscillators, we extended the mean-field approach to networks of heterogeneous oscillators. This was accomplished through the derivation of three separate mean-field systems, MFI, MFII and MFIII, with differing applications and regions of validity. We successfully applied numerical bifurcation analysis to MFI and MFII to aid in the understanding of the different behaviors that heterogeneous networks can display, and how they transition between these different types of behaviors. More importantly however, we have surpassed the natural limitation of mean-field systems: that they can only provide information about the first moments. With a few additional tools, we used MFIII to derive information about distributions of firing rates, and even parameters, given some basic knowledge.

Other researchers [11, 31] have derived firing rate distributions for heterogeneous networks, however these have been derived under differing assumptions. For example, the heterogeneous mean field systems studied by Hansel and Mato (Equations (5.5)-(5.7) in [11]) have similar integral terms to our MFII however they are firing rate models. Our models are current/conductance based models. The difference between these two types of equations arises from which time scale is the fastest, that of the synaptic current, or the firing rate. If the firing rate time scale is assumed to be the fastest, then a differential equation for the synaptic current can be obtained (as in our case). If the time scale of the synaptic current is assumed to be the fastest, then one obtains firing rate equations, as in [11]. The fact that these two different limits result in different kinds of equations were first highlighted in [5] (section 7.2). Additionally, no adaptation is contained in the rate models in [11]. Finally, it is likely that the firing rate models shown in [11] cannot display period doubling bifurcations as they have a similar structure to MFII, which misses out on the more complicated bifurcations of the actual network that MFIII can reproduce, due to its PDE nature.

The model of Vladimirov et al. [31] is formulated in terms of an input-output relation for the synaptic conductance, so has a different structure than ours. It involves a distribution of the synaptic depression variable so has some aspects similar to our MFIII, however, no PDE governing the evolution of this variable is derived.

Dur-e-Ahmad et al. [8] studied adaptation induced bursting in a network of homogeneous Izhikevich neurons, with parameters determined from experimental data on CA3 pyramidal neurons. They showed that, if the adaptation is strong enough, network bursting occurs in large regions of the parameter space consisting of the synaptic conductance, g_{syn} , and the applied current, I_{app} . In [19] we showed that the transition from tonic firing to bursting involves a saddle-node bifurcation of non-smooth limit cycles, followed by a grazing bifurcation and a subcritical Hopf bifurcation. For fixed I_{app} greater than rheobase but sufficiently small, there is one transition from tonic firing to bursting at a low g_{syn} value and another from bursting back to tonic firing at a higher g_{syn} value. Thus the bursting region is a closed semi-circular region in the g_{syn}, I_{app} parameter space. In [19] we showed that the size of this bursting region is reduced if the network is

split into two homogeneous subnetworks, one strongly adapting and one weakly adapting. Here, we used the tools we developed to investigate how this adaptation induced network bursting is affected by heterogeneity in the parameters. Somewhat surprisingly, we have found that adaptation induced network bursting is not very robust to heterogeneity. This has been confirmed by direct simulations of the full network, bifurcation analysis using MFII and analysis of the proportion of bursting neurons in the network using MFIII. This lack of robustness is caused by two changes to the homogeneous case:

1. The low g_{syn} Hopf bifurcation point moves towards higher values, thereby decreasing the size of the bursting region
2. The low g_{syn} Hopf bifurcation switches from subcritical to supercritical. This has two effects:
 - the bifurcation direction changes, eliminating the bursting at conductance values less than the bifurcation value
 - the initial limit cycles created by the bifurcation are small amplitude oscillations in the firing rate as opposed to full bursts, thus the transition to bursting moves to even higher conductance values.

Further, in networks with both weakly and strongly adapting neurons, heterogeneity caused the high g_{syn} Hopf bifurcation value to decrease when the proportion of strongly adapting neurons is reduced.

Let us now put our results in the context of experimental results on the CA3 region. Bursting is often seen in these studies [2, Section 5.3.5]. When the neurons have their synaptic inputs blocked however, the majority ($\approx 80\%$) of these pyramidal neurons do not display bursting, but different degrees of spike frequency adaptation [12]. Thus, it would seem that adaptation induced network bursting should play a role in the CA3 network. However, the biophysically important part of the parameter region is in the low g_{syn} region [19]. When this fact is taken in conjunction with our results described above, this would seem to weaken the case that adaptation induced network bursting is the only source of bursting in CA3 networks. Some other mechanism seems necessary.

In their study of hippocampal CA3 pyramidal neurons, Hemond and colleagues note that roughly 20% of pyramidal neurons were intrinsically bursting. That is, the neurons burst without any synaptic input for some input current. It may be possible that a small subpopulation of intrinsically bursting neurons can facilitate bursting in the rest of the network, however this would depend on the conductance values connecting this particular subpopulation to the rest of the network. This hypothesis can be tested relatively easily using a mean-field approach. All that is required is to fit a two-dimensional adapting model to the intrinsically bursting neurons. This is feasible, as has been previously noted, all the two-dimensional adapting neurons can be turned into intrinsically bursting neurons by simple parameter changes [13]. The conductance parameter connecting this subpopulation to the rest is best treated as a bifurcation parameter, with some estimate of the range in which it lies in from physiological data.

While an intrinsically bursting subpopulation is the most promising avenue of study with regards to hippocampal bursting, synaptic depression has also been shown to induce bursting in oscillators that cannot otherwise display this behavior. In a model of the developing chick spinal cord, [31] found that heterogeneity actually makes the bursting more robust, as opposed to less as we have found. Thus it is possible the synaptic depression induced bursting is more robust to heterogeneity than adaptation induced bursting. However, in this study the heterogeneity was via a uniform distribution in the applied current (as opposed to the Gaussian distributions we consider) and typically $\langle I_{app} \rangle$ was close to rheobase, which could also be factors in their results.

In addition to area CA3 in the hippocampus, adaptation induced bursting has also been suggested as a possible mechanism for the generation of velocity controlled oscillators (VCO's) in the entorhinal cortex by [33]. The VCO's burst at frequencies that vary with the velocity of the animal. When a subset of VCO's signals are linearly added to a readout neuron, an interference pattern emerges and a grid cell is formed. [33] use a recursively coupled network of homogeneous Izhikevich neurons with adaptation variables given by $W_{jump} = 100$, and $1/\tau_W = 0.03$, and these parameters are strong enough so that adaptation induced bursting can occur. The network acts a single velocity controlled oscillator, and the burst frequency is set to vary with the velocity of an animal. This is done by fixing the g_{syn} parameter at a specific value, and

inverting the $F(I)$ curve where F is the frequency of bursts, and I is the homogenous applied current to each neuron. Grid cells can be generated by using multiple networks and linearly adding their output currents to a read-out neuron. This was done under uncorrelated noisy inputs arriving to each neuron. However, [33] state that synchrony in the noise (which can come from the animals velocity signal for example) coming to each VCO network can disrupt grid-cell formation. Here, we have shown that a heterogeneous network of oscillators can still maintain a network level oscillation rate, even if the individual neurons have different behaviors. The network level behaviors are predicted from the mean-field systems. Given the fact that the individual neurons are heterogeneous, any synchronized noise input into the individual neurons should become increasingly desynchronized by the differing responses of the individual neurons. As a network level oscillation exists and the heterogeneity will likely desynchronize any noise coming to the individual oscillators, this is a plausible means of generating velocity controlled oscillators. We leave this particular application of mean-field theory for future work.

In either of these applications, a mean-field system may yield valuable insights as to the mechanisms of bursting and the parameter regions they occur in. By carefully choosing the appropriate bifurcation parameters, and accounting for the level of heterogeneity in the neurons in the network, one can determine the bifurcation types and behaviors neurons in these different networks display, in addition to estimates of the different distributions to yield insights about the real cells.

Appendix A: Computing $\langle v \rangle$ and $\langle v | \beta \rangle$

When the quasi-steady state approximation is applicable, a very convenient method emerges for computing the moments of v . In particular, the quasi-steady state approximation not only yields the steady state flux, but it also yields the steady state density:

$$\rho(v) = \frac{J(s, \langle w \rangle)}{F(v) - \langle w \rangle + gs(e_r - v) + I}$$

where $J(s, \langle w \rangle)$ is the steady state flux ($\langle R_i(t) \rangle$ for $H(\langle w \rangle, s) \geq 0$). Obviously with the density, we can compute the moments of any arbitrary function of v . For example, $\langle v \rangle$ is given by

$$\langle v \rangle = \int_V \frac{J(s, \langle w \rangle) v dv}{F(v) - \langle w \rangle + gs(e_r - v) + I} \quad \text{if } H(s, \langle w \rangle) \geq 0 \quad (80)$$

However, once we cross the switching manifold, equation (80) is no longer valid. An approximation has to be made to compute $\langle v \rangle$ in this region. In particular, we will assume that $\langle F(v) \rangle = F(\langle v \rangle)$, and that the dynamics of $\langle v \rangle$ are fast relative to s and $\langle w \rangle$. If so, then the dynamics of $\langle v \rangle$ are approximately given by

$$\langle v \rangle' \approx F(\langle v \rangle) - \langle w \rangle + gs(e_r - \langle v \rangle) + I \quad (81)$$

and we can solve the steady state equation for $\langle v \rangle$

$$F(\langle v \rangle) - \langle w \rangle + gs(e_r - \langle v \rangle) + I = 0$$

However, we have to be careful here. Based on the assumptions on $F(v)$ we know that there are only two solutions to this system, and we need to solve for the stable one. For the Izhikevich neuron for example, this is given by

$$\langle v_- \rangle = \frac{\alpha + gs}{2} - \sqrt{-H(s, \langle w \rangle)} \quad (82)$$

Computation of the integral for the Izhikevich neuron, in conjunction with equation 82 yields the following equation for $\langle v \rangle$ over the entire $s, \langle w \rangle$ plane:

$$\langle v \rangle = \begin{cases} \frac{\langle R_i(t) \rangle}{2} \log \left(\frac{(v_{peak} - \frac{\alpha + gs}{2})^2 + H(s, w)}{(v_{reset} - \frac{\alpha + gs}{2})^2 + H(s, w)} \right) + \frac{\alpha + gs}{2} & : H(\langle w \rangle, s) \geq 0 \\ \frac{\alpha + gs}{2} - \sqrt{-H(s, w)} & : H(\langle w \rangle, s) < 0 \end{cases} \quad (83)$$

The same formulas can actually be used for $\langle v|\boldsymbol{\beta} \rangle$, with the interpretation that they are now explicit functions of $\boldsymbol{\beta}$. In particular, one can show that under tonic firing, $\langle v|\boldsymbol{\beta} \rangle$ is given by the same formula as $\langle v \rangle$ when $H(\langle w \rangle, s, \boldsymbol{\beta}) \geq 0$. Additionally, the formula for $\langle v \rangle$ for $H(s, \langle w \rangle, \boldsymbol{\beta}) < 0$ is also a satisfactory approximation for $\langle v|\boldsymbol{\beta} \rangle$. To once again reiterate that while the formula for the mean $\langle v|\boldsymbol{\beta} \rangle$ under heterogeneity is the same as the formula for $\langle v \rangle$ under homogeneity, this does not imply that $\langle v \rangle = \langle v|\boldsymbol{\beta} \rangle$. In fact, to compute $\langle v \rangle$, one has to compute the traditional integral for it:

$$\langle v \rangle = \int_{\boldsymbol{\beta}} \langle v|\boldsymbol{\beta} \rangle \rho_{\boldsymbol{\beta}}(\boldsymbol{\beta}) d\boldsymbol{\beta}$$

Appendix B: Computing the Proportion of Bursting Neurons in Direct Simulations

Performing direct simulations of a network is fairly straight forward, but it is somewhat difficult to use the results of the simulations to automatically classify a given neuron, let alone the entire network, as bursting or tonically firing. We considered various classifiers and opted to use the ratio of the largest to the smallest interspike interval for a neuron when the network has reached steady state. For a bursting neuron, the ratio of its largest interspike interval (which is the interburst interval) to its smallest interspike interval should be large. Thus for the i^{th} neuron we define

$$\lambda_i = \frac{\max ISI}{\min ISI} \quad (84)$$

where the max/min is determined after a suitable time period of steady state behaviour (either bursting or tonically firing). We set a critical ratio, λ_c , and classify neuron i as bursting if λ_i is higher than this ratio. The critical ratio is typically taken to be 2. This is the single neuron classifier. We use the single neuron classifier to make an estimate for the total proportion of bursting neurons in the network as follows

$$p_{burst} = \frac{1}{N} \sum_{i=1} H(\lambda_i - \lambda_c) \quad (85)$$

where H is the Heaviside function. We can use p_{burst} to classify a network by picking some specific critical value of p_{burst} as a threshold for a classifier, however it is more informative to simply plot the contours of p_{burst} for a set of simulations run over a mesh in the bifurcation parameters of interest.

Appendix C: Multiple Subpopulations via Mixed Distributions of Heterogeneity

In [19] we considered multiple subpopulations for heterogeneous networks by simulating discrete homogeneous subpopulations within a network. For example, we simulated two subpopulations with two different sets of parameters corresponding to weakly adapting and strongly adapting neurons as a first attempt at studying inhomogeneous networks. However, a more realistic way of analyzing subpopulations in heterogeneous networks, is through the use of mixed distributions. A mixed random variable Z is a function of two or more random variables. For example, if X and Y are random variables with probability density functions f_X and f_Y , respectively, then

$$Z = \begin{cases} X & \text{with probability } p \\ Y & \text{with probability } 1 - p \end{cases} \quad (86)$$

is a mixed random variable with probability density function

$$f_Z(z) = pf_X(z) + (1 - p)f_Y(z). \quad (87)$$

Now consider a network where the adaptation jump size w_{jump} comes from two different subpopulations. In one subpopulation, $\langle w_{jump} \rangle$ is large, and in the other, $\langle w_{jump} \rangle$ is small. We can simulate these two subpopulations within an individual (all-to-all) coupled network using heterogeneity, and the density function

$$f_{w_{jump}}(w) = p_{SA}f_{SA}(w) + (1 - p_{SA})f_{WA}(w) \quad (88)$$

where p_{SA} denotes the proportion of strongly adapting neurons and SA denotes the strongly adapting subpopulation, and WA denotes the weakly adapting subpopulation. Note that these densities have higher moments than simply $\langle w_{jump} \rangle$, and it is the magnitude of these moments that determine whether or not the density in the heterogeneous parameter we are considering is bimodal, indicative of multiple subpopulations. Using this approach we can analyze how the bimodality affects the steady state distribution properties. We can also use more of the data gained from real networks for the purposes of simulation, as opposed to arbitrarily classifying neurons as strongly adapting or weakly adapting. The parameters of the individual density functions can be approximated, along with p , using standard statistical approaches (maximum likelihood estimation, for example). More importantly however, the same mean-field equations apply to a unimodal or a multimodal distribution of heterogeneity.

Appendix D: Differentiation and Numerical Inversion of Parameter Distributions

The procedure in section 3.2.2 requires not only the estimation of $\langle R_i | \beta \rangle$, but also the calculation of its inverse and the derivative of this inverse. To calculate $\langle R_i | \beta \rangle$ the mean field equations (57)-(59) are discretized in β and the resulting equations are numerically integrated to steady state, which yields the steady state value of $\langle R_i | \beta_j \rangle$ at each mesh point, β_j . The inverse $g^{-1}(r)$ is calculated via numerically inverting the steady state $\langle R_i | \beta_j \rangle$ as a function of β_j as follows. The MATLAB function `interp1` is used to interpolate values of β given values of R using the steady state $(\langle R_i | \beta_j \rangle, \beta_j)$ mesh points. The derivative of the inverse is calculated using a finite-difference approximation over the mesh:

$$\left. \frac{dg^{-1}}{dr} \right|_{r=r_j} \approx \frac{g^{-1}(r_{j+1}) - g^{-1}(r_j)}{r_{j+1} - r_j}$$

This is then used to find $\rho_R(r)$ at each mesh point via equation (62).

To implement the computations in section 3.2.3, equations (77)-(78) are discretized in β and numerically integrating to compute the steady state value of $\langle R_i | \beta \rangle$ at each mesh point, $\langle R_i | \beta_j \rangle$. This is then used to compute $\frac{d}{d\beta} \langle R | \beta \rangle$ through a first order finite-difference approximation over the discrete mesh:

$$\left. \frac{d\langle R_i | \beta \rangle}{d\beta} \right|_{\beta=\beta_j} \approx \frac{\langle R_i | \beta_{j+1} \rangle - \langle R_i | \beta_j \rangle}{\beta_{j+1} - \beta_j}.$$

These two quantities are then used as approximations of $g(\beta)$ and $g'(\beta)$ in equation (72) to find $\rho_{beta}(\beta)$ at each mesh point.

To estimate the parameter values for individual neurons, we take the discretized steady state firing rate, $\langle R_i | \beta_j \rangle$, calculated as indicated above. We then invert the functional relationship between $\langle R_i | \beta_j \rangle$ and β_j , and interpolate the β values of the individual neurons using their firing rate, i.e., we treat $\langle R_i | \beta_j \rangle$ and β_j as the (x_j, y_j) points to be interpolated. This yields an estimate of the parameter values for each individual neuron, unlike in the approach for section 3.2.2 which yielded an estimate of the overall distribution. Note that all that is required for this computation is knowledge of the steady state firing rate for each neuron. We use the `griddata` and the `interp1` functions in MATLAB to perform the interpolation.

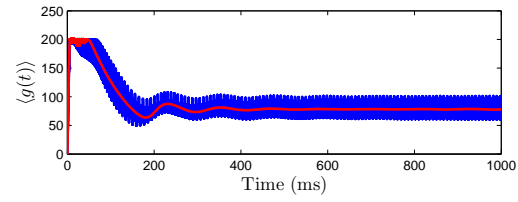
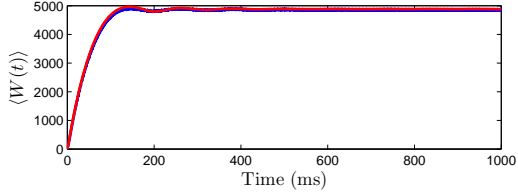
Acknowledgements

This work benefitted from the support of the Natural Sciences and Engineering Research Council of Canada and the Ontario Graduate Scholarship program

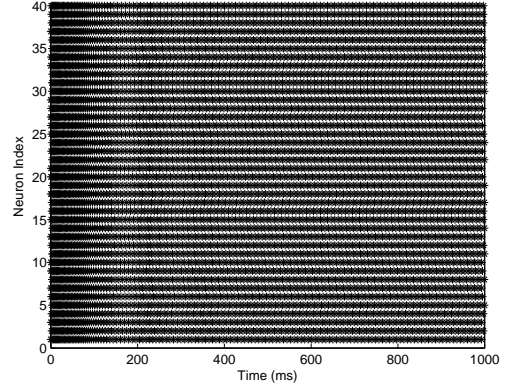
References

- [1] L.F. Abbott and C. van Vreeswijk. Asynchronous states in networks of pulse-coupled oscillators. *Learning and Memory*, 48(2):1483–1490, 1993.
- [2] P. Andersen, R. Morris, D. Amaral, T. Bliss and J. O’Keefe (Eds). The hippocampus book. Oxford University Press, Oxford UK, 2006.
- [3] P.C. Bressloff. Spatiotemporal dynamics of continuum neural fields *Journal of Physics A: Mathematical and Theoretical*, 45(3):033001, 2012.
- [4] G. Buzsáki Large-scale recordings of neuronal ensembles. *Nature Neuroscience*, 7(5):446–451, 2004.
- [5] P. Dayan, and L.F. Abbott. Theoretical Neuroscience *MIT Press, Cambridge Massachusetts*, 2001.
- [6] A. Dhooge, W. Govaerts, and Yu. A. Kuznetsov. MATCONT: A MATLAB package for numerical bifurcation analysis of ODEs. *ACM Transactions on Mathematical Software*, 29(2):141–164, 2003.
- [7] M. di Bernardo, C.J. Budd, A.R. Champneys, P. Kowalczyk, A.B. Nordmark, G.O. Tost, and P.T. Piironen. Bifurcations in nonsmooth dynamical systems. *SIAM Review*, 50(4):629–701, 2008.
- [8] M. Dur-e-Ahmad, W. Nicola, S.A. Campbell, and F. Skinner. Network bursting using experimentally constrained single compartment CA3 hippocampal neuron models with adaptation. *Journal of Computational Neuroscience*, 33(1): 21–40, 2012.
- [9] B.F. Grewe, D. Langer, H. Kasper, B.M. Kampa and F. Helmchen. High-speed *in-vivo* calcium imaging reveals neuronal network activity with near-millisecond precision *Nature Methods*, 7(5): 399–405, 2010.
- [10] D. Hansel, and G. Mato. Existence and stability of persistent states in large neuronal networks. *Phys. Rev. Lett.*, 86(18): 4175–4718, 2001.
- [11] D. Hansel, and G. Mato. Asynchronous states and the emergence of synchrony in large networks of excitatory and inhibitory neurons. *Neural Computation*, 15(1):1–56, 2003.
- [12] P. Hemond, D. Epstein, A. Boley, M. Migliore, G.A. Ascoli, and D.B. Jaffe. Distinct classes of pyramidal cells exhibit mutually exclusive firing patterns in hippocampal area CA3b. *Hippocampus*, 18(4):411–424, 2008.
- [13] E.M. Izhikevich. Simple model of spiking neurons. *Neural Networks, IEEE Transactions on*, 14(6):1569 – 1572, 2003.
- [14] E.M. Izhikevich and G.M. Edelman Large-Scale Model of Mammalian Thalamocortical Systems *PNAS*, 105:3593–3598, 2008.
- [15] B.W. Knight. Dynamics of encoding in neuron populations: Some general mathematical features. *Neural Comput.*, 12(3):473–518, 2000.
- [16] C. Ly and D. Tranchina. Critical analysis of dimension reduction by a moment closure method in a population density approach to neural network modeling. *Neural Computation*, 19(8):2032–2092, 2007.
- [17] MATLAB. *version 7.10.0 (R2012a)*. The MathWorks Inc., Natick, Massachusetts, 2012.
- [18] R. Naud, N. Marcille, C. Clopath, and W. Gerstner. Firing patterns in the adaptive exponential integrate-and-fire model. *Biological Cybernetics*, 99:335–347, 2008.
- [19] W. Nicola, and S.A. Campbell. Bifurcations of large networks of two-dimensional integrate and fire neurons *Journal of Computational Neuroscience*, 35: 87–108, 2013.

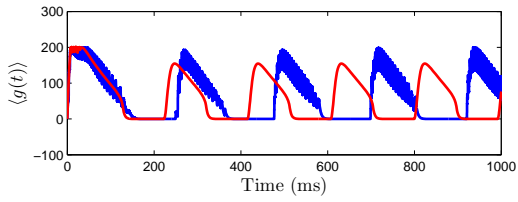
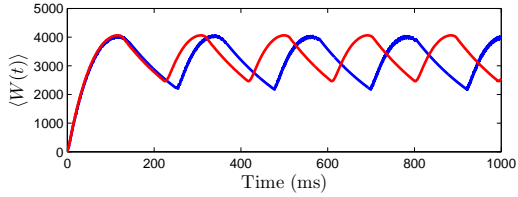
- [20] D.Q. Nykamp. and D. Tranchina. A population density approach that facilitates large-scale modeling of neural networks: Analysis and an application to orientation tuning. *Journal of Computational Neuroscience*, 8:19–50, 2000.
- [21] A. Omurtag, B.W. Knight, and L. Sirovich. On the simulation of large populations of neurons. *Journal of Computational Neuroscience*, 8:51–63, 2000.
- [22] L. Renyi Probability Theory *North-Holland Publishing Company, Amsterdam*, 1970.
- [23] L. Sirovich, A. Omurtag, and B. W. Knight. Dynamics of neuronal populations: The equilibrium solution. *SIAM Journal on Applied Mathematics*, 60(6):pp. 2009–2028, 2000.
- [24] J. E. Lisman. Bursts as a unit of neural information: making unreliable synapses reliable *Trends in Neuroscience*, 20(1):pp. 38–43, 1997.
- [25] L. Sirovich, A. Omurtag, and K. Lubliner. Dynamics of neural populations: Stability and synchrony. *Network: Comput. Neural Syst*, 17(1):3–29, 2006.
- [26] F.K. Skinner, H. Bazzazi and S.A. Campbell Two-Cell to N-Cell Heterogeneous, Inhibitory Networks: Precise Linking of Multistable and Coherent Properties0 *J. Computational Neuroscience* 18(3): 343-352.
- [27] S.H. Strogatz and R. E. Mirollo. Stability of incoherence in a population of coupled oscillators. *Journal of Statistical Physics*, 63:613–635, 1991.
- [28] J. Touboul. Bifurcation analysis of a general class of nonlinear integrate-and-fire neurons. *SIAM Journal on Applied Mathematics*, 68(4):1045–1079, 2008.
- [29] C. van Vreeswijk. Partial synchronization in populations of pulse-coupled oscillators. *Phys. Rev. E*, 54(5):5522–5537, 1996.
- [30] C. van Vreeswijk, L.F. Abbott., and B.G. Ermentrout. When inhibition not excitation synchronizes neural firing. *Journal of Computational Neuroscience*, 1:313–321, 1994.
- [31] B.B. Vladimirovski, J. Tabak, M.J. O’Donovan, J. Rinzel (2008) Episodic activity in a heterogeneous excitatory network, from spiking neurons to mean field. *Journal of Computational Neuroscience* 25:39–63
- [32] C. van Vreeswijk and D. Hansel. Patterns of synchrony in neural networks with spike adaptation. *Neural Computation*, 13(5):959–992, 2001.
- [33] E.A. Zilli and M.E. Hasselmo. Coupled noisy spiking neurons as velocity controlled oscillators in a model of grid cell spatial firing *The Journal of Neuroscience*, 30(41):13850–14860, 2010.



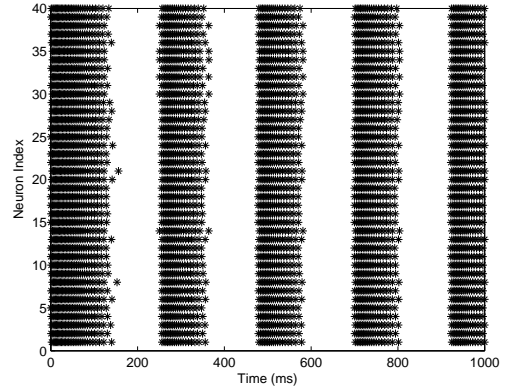
(a) $I_{app} = 4500$ pA, $g_{syn} = 200$ nS



(b) Spike time raster plot for (a)



(c) $I_{app} = 3500$ pA, $g_{syn} = 200$ nS



(d) Spike time raster plot for (c)

Figure 1: Numerical simulation of a homogeneous network of 1000 Izhikevich neurons, with parameters as shown. The rest of the parameters can be found in Table 1. Simulations of the mean-field equations (in red) and the mean values of the corresponding full network simulations (in blue) showing (a) tonic firing and (b) bursting. (b),(d) Raster plots for 40 randomly selected neurons from the network simulation in (a),(c). The mean-field equations are fairly accurate both when the network is tonically firing and when it is bursting.

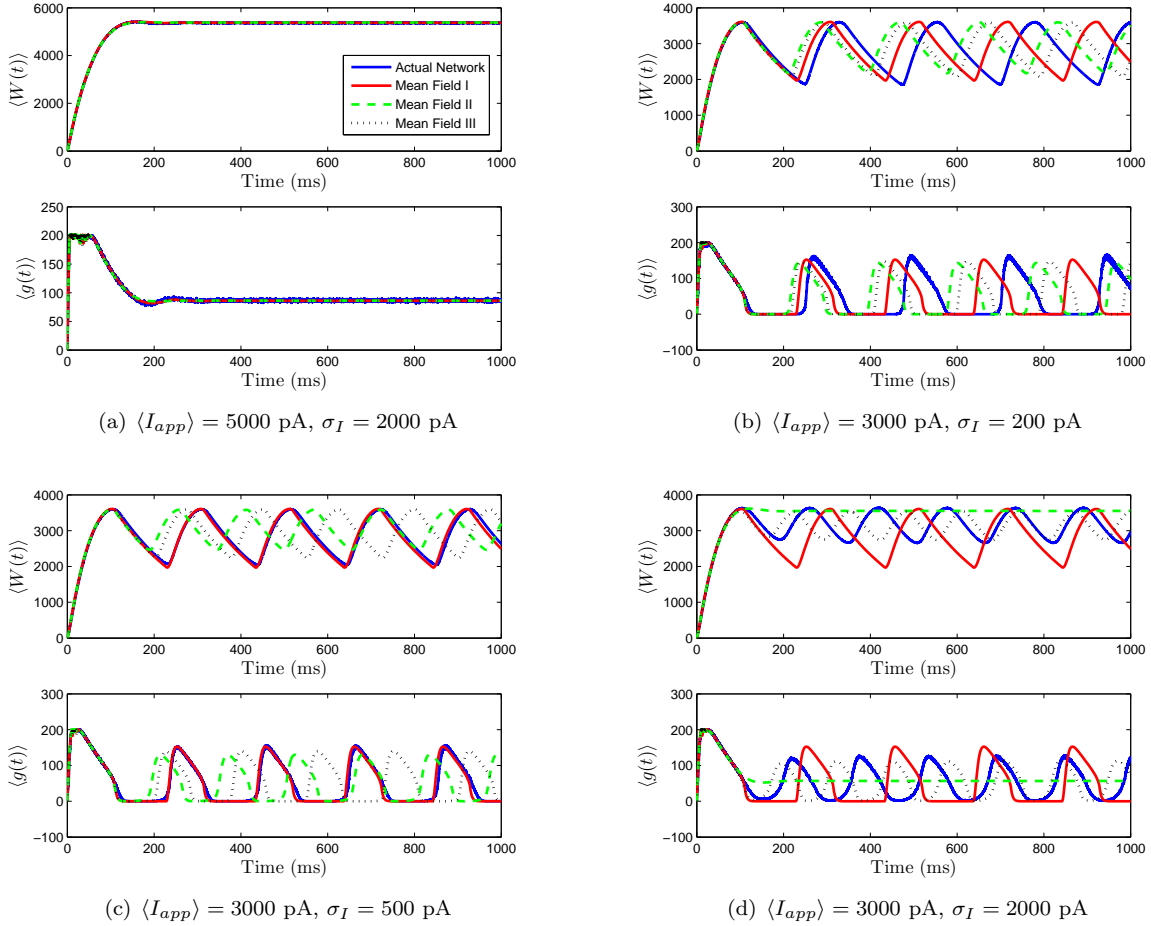


Figure 2: Numerical simulations of a network of 1000 Izhikevich neurons with parameters as in Table 1, except $g_{syn} = 200$ and the applied current which is normally distributed with mean and variance as shown. Blue is the network average of a given variable, red is MFI, green is MFII and black is MFIII. In this region, the mean-driving current is away from rheobase, $\langle I_{app} \rangle \gg I_{rh}$. All three approximations are quantitatively and qualitatively similar for small to intermediate sized variances in the distribution of currents. For small variances, MFI is the most accurate and for larger variances, MFIII is the most accurate. For large variance, MFII bifurcates back to tonic firing earlier than MFI and MFIII, as seen in (d)

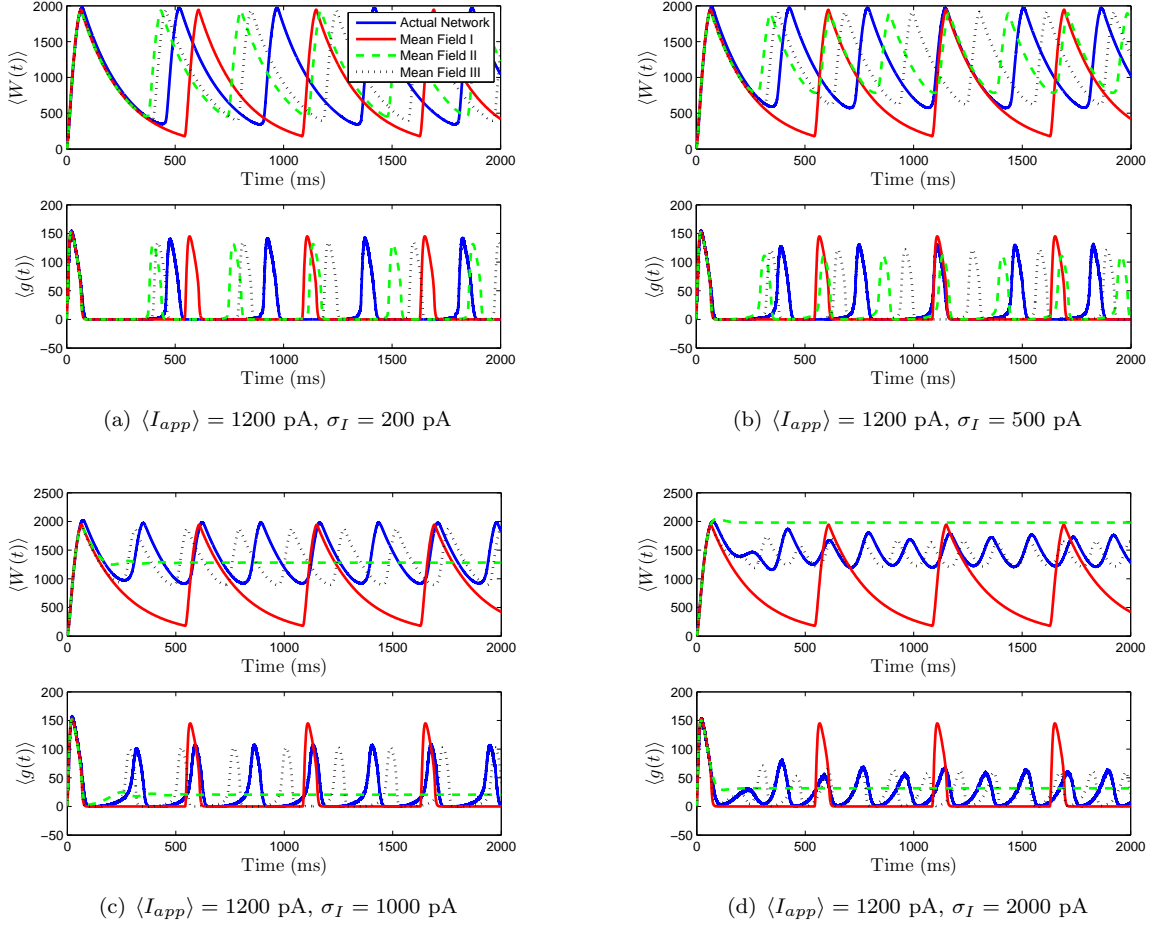
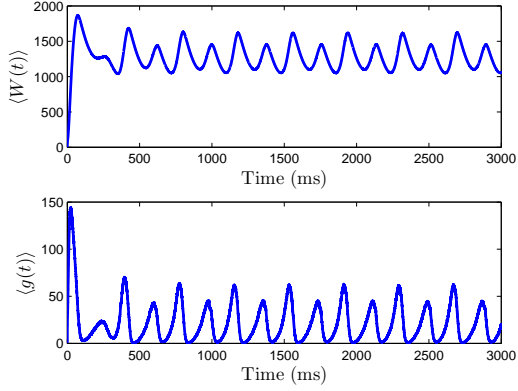
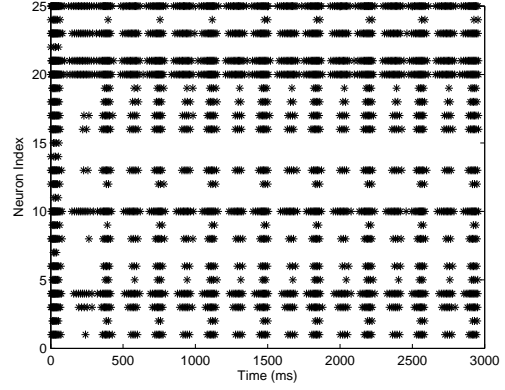


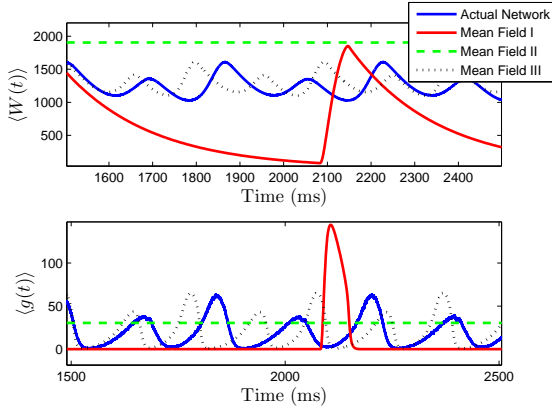
Figure 3: Numerical simulations of a network of 1000 neurons with parameters as in Table 1, except $g_{syn} = 200$ and the applied current which is normally distributed with mean and variance as shown. Blue is the network average of a given variable, red is MFI, green is MFII and black is MFIII. In these simulations, the mean-driving current is close to (and over) the rheobase. In all cases, MFI is the least accurate. This is because it depends only on $\langle I_{app} \rangle$. When $\langle I_{app} \rangle = O(I_{rh})$, even for small variance, many of the neurons have $I < I_{rh}$ and may not spike at all. (a),(b) For small values of σ_I , all three approximations are qualitatively and quantitatively accurate. (c),(d) For larger variance, $\sigma_I = O(I_{rh})$, only MFIII is qualitatively and quantitatively accurate. In this case, MFII bifurcates early to tonic firing.



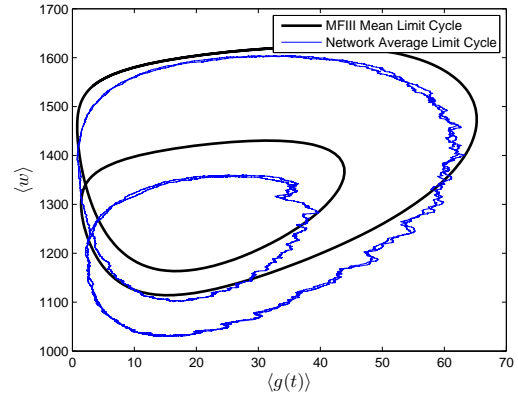
(a) $\langle I_{app} \rangle = 1100$ pA, $\sigma_I = 2000$ pA



(b) Raster plot of the simulation

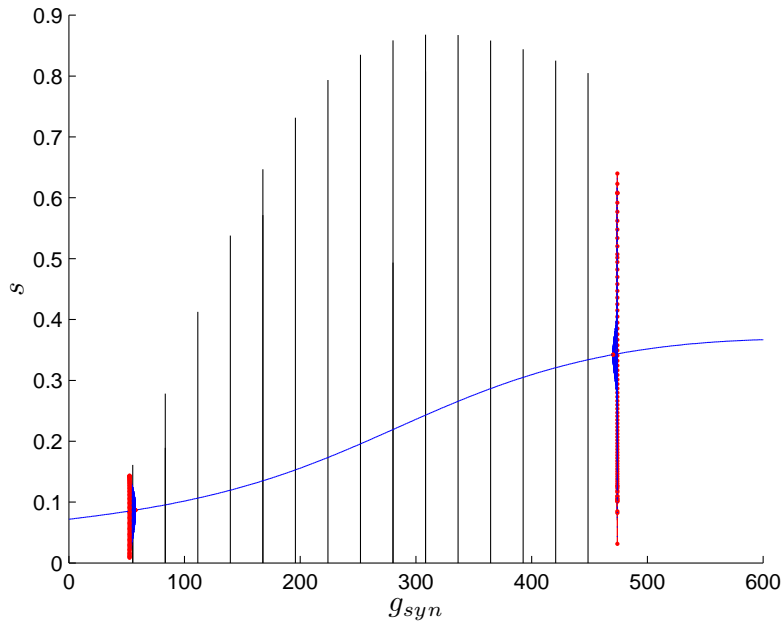


(c) Mean-field equations at same parameter values

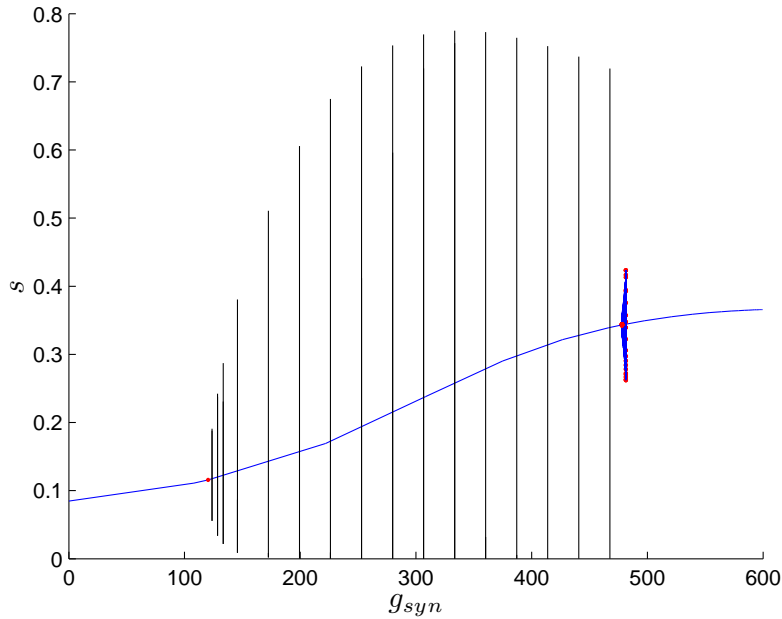


(d) Steady state period doubled limit cycle

Figure 4: Period doubled limit cycle in the heterogeneous network and in MFIII. The network consists of 5000 neurons, with parameters as in Table 1, except $g_{syn} = 200$ and the applied current which is normally distributed with mean and variance as shown in (a). (a) period-doubled limit cycle for the network shown in terms of the mean variables. (b) raster plot of 25 randomly selected neurons of the network. The behaviors include burst firing, alternate burst firing, tonic firing, and quiescence. (c) numerical simulations of the mean-field systems. Only MFIII is able to reproduce the period doubling behavior. (d) Comparison of the “phase portrait” of period doubled limit cycle for MFIII and the mean variables of network.

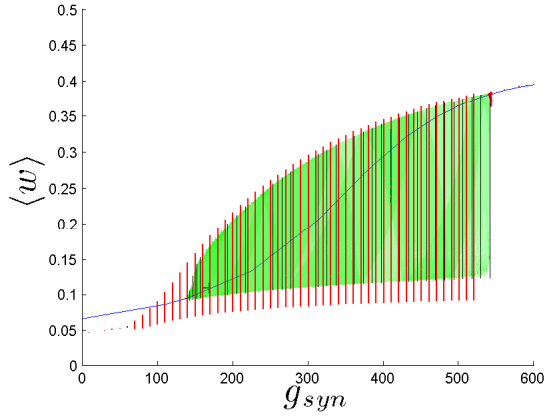


(a) MFI, $I_{app} = 2000$ pA

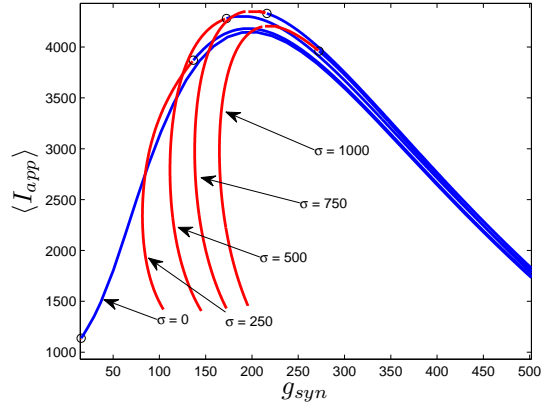


(b) MFII, $\langle I_{app} \rangle = 2000$ pA, $\sigma_I = 500$ pA

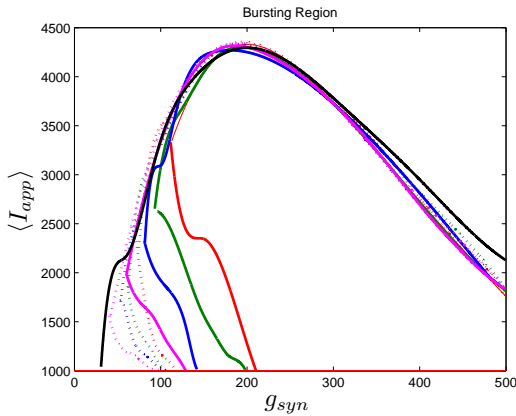
Figure 5: Comparison between the bifurcation structure of homogeneous and heterogeneous networks using mean-field models. The parameters are as in Table 1, except the applied current which is normally distributed with mean and variance as shown and g_{syn} which varies as shown. Blue curve is equilibrium point, vertical black/blue lines denote stable/unstable periodic orbits. Red dots denote bifurcation points. (a) Homogeneous case. Numerical bifurcation analysis of MFI displays two subcritical Hopf bifurcations: one at a low g_{syn} value and one at a high value. (b) Heterogeneous case. Numerical bifurcation analysis of MFII also displays two Hopf bifurcations, but the one at the low g_{syn} value is supercritical. This makes bursting at low g_{syn} values less robust in the heterogeneous case as discussed in the text.



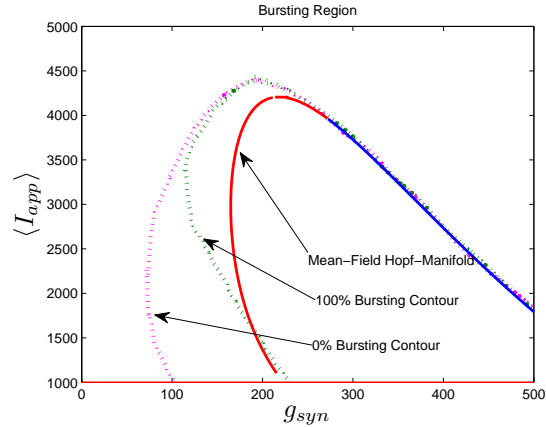
(a) Hopf bifurcation from MFII and full network simulations with $\langle I \rangle = 1500$, $\sigma_I = 500$



(b) Hopf manifolds determined from mean-field models

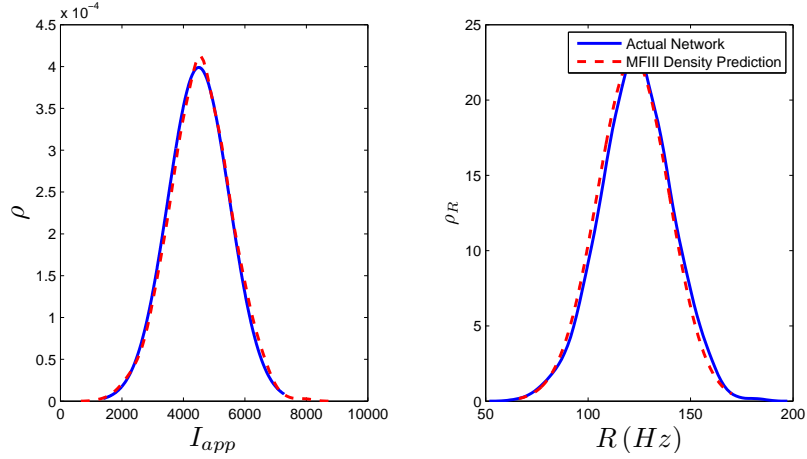


(c) Bursting regions from full network simulations

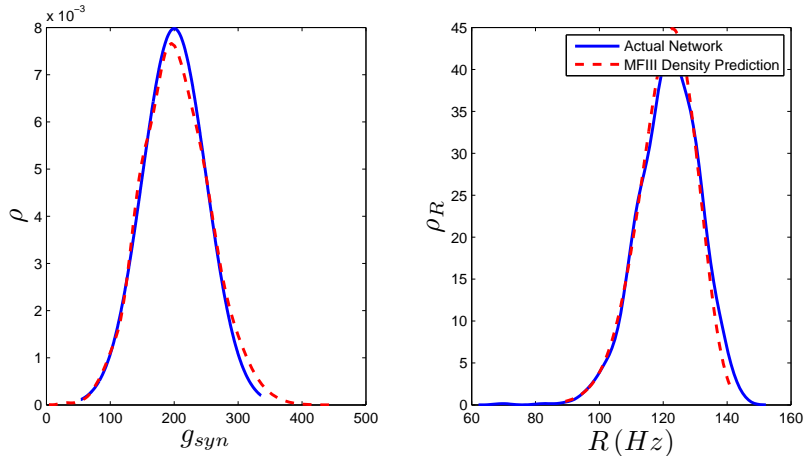


(d) Bursting region from MFII and full network simulations with $\sigma_I = 1000$

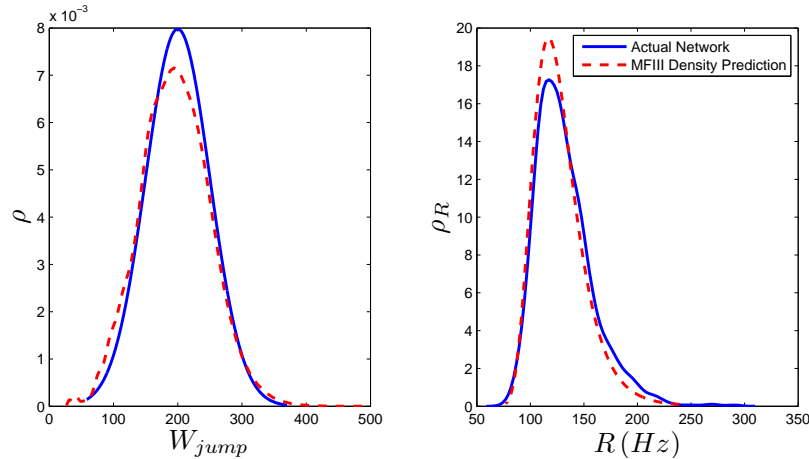
Figure 6: Comparison between numerical bifurcation analysis of MFII and direct simulation of the full network. The parameters are as in Table 1, except g_{syn} varies as discussed below and the applied current which is normally distributed with mean and variance as discussed below. (a) Simulations of a network of 10,000 neurons with $\langle I_{app} \rangle$ and σ_I as shown were run at discrete values of g_{syn} for 2000 ms. The last 400 (ms) of simulation time is plotted (in red), showing the stable limit cycle oscillation for different g_{syn} values. This is compared to numerical continuation of the MFII limit cycle and equilibrium (in green and blue). Both the actual network and MFII appear to undergo a supercritical Hopf bifurcation for low g values and a subcritical Hopf for high g values. (b) The Hopf manifolds for the mean-field systems with σ_I as shown. Red denotes supercritical Hopf bifurcations, and blue denote subcritical Hopf bifurcations. The black circles denote codimension 2 Bautin bifurcation points. (c) Simulations of a network of 1000 neurons run on a discrete mesh of $\langle I_{app} \rangle$ and g_{syn} values. The 0% (dotted line) and 100% (solid line) network bursting contours for $\sigma_I = 0, 250, 500, 750$, and 1000 pA are coloured in black, magenta, blue, green, and red, respectively. The curves are spline fits to the actual contours. (d) MFII Hopf manifold and spline fits to the 0% bursting and 100% bursting contours of the actual network for $\sigma_I = 1000$.



(a) Distribution of I_{app} with $\langle I_{app} \rangle = 4500$ pA, $\sigma_I = 1000$ pA

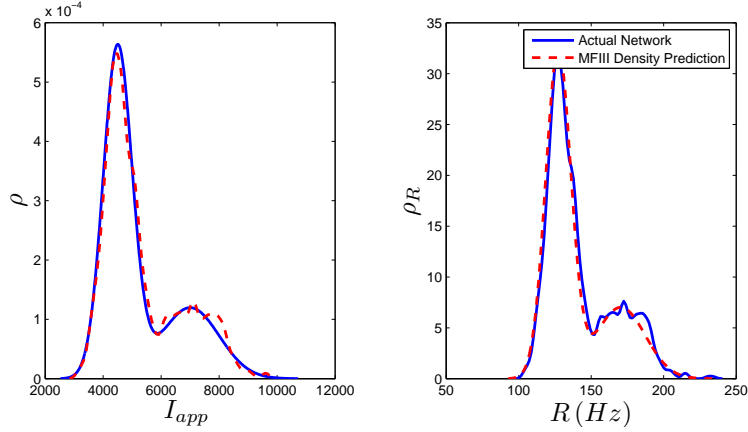


(b) Distribution of g_{syn} with $\langle g_{syn} \rangle = 200$ nS, $\sigma_g = 50$ nS

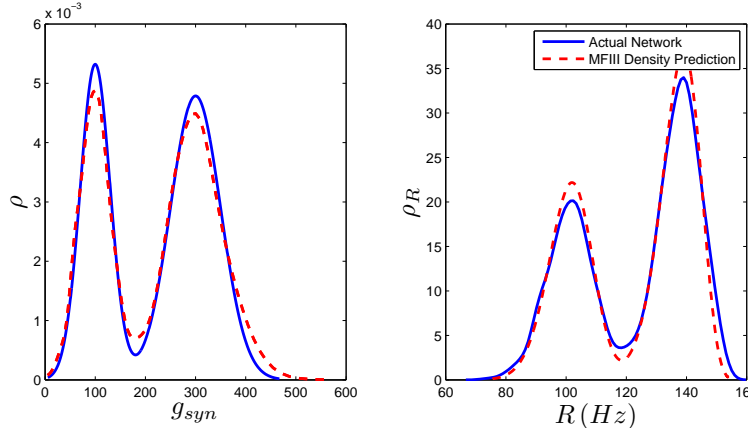


(c) Distribution of W_{jump} with $\langle W_{jump} \rangle = 200$ pA, $\sigma_W = 50$ nS

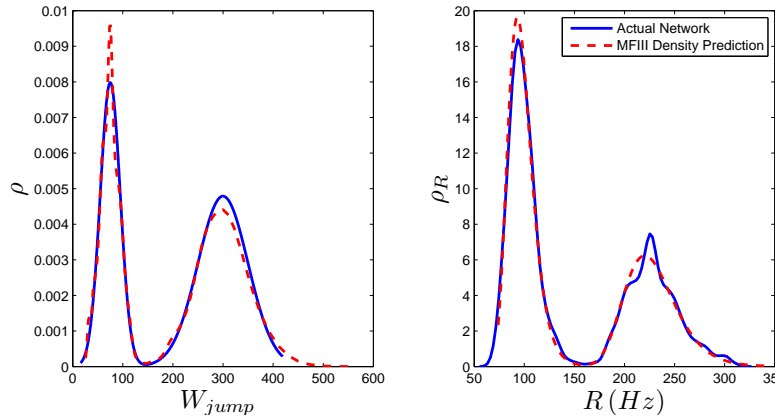
Figure 7: Heterogeneity in I_{app} , g_{syn} , or W_{jump} leads to heterogeneity in the firing rate. As described in section 3.2.2, given the parameter distribution (solid curves, left column) MFIII can be used to estimate the corresponding distribution of firing rates in the network (dashed curves, right column). As described in section 3.2.3, given the the steady state firing rate distribution of an actual network (solid curves, right column) MFIII can be used to estimate the parameter distribution in the network (dashed curves, left column). The network firing rate distribution is estimated using a histogram. The calculations were carried out on a network of 1000 neurons. Parameters, other than those indicated, can be found in Table 1.



(a) Distribution of I_{app} with $\mu_1 = 4500$ pA, $\sigma_1 = 500$ pA, $\mu_2 = 7000$ pA, $\sigma_2 = 1000$ pA, $m = 0.7$

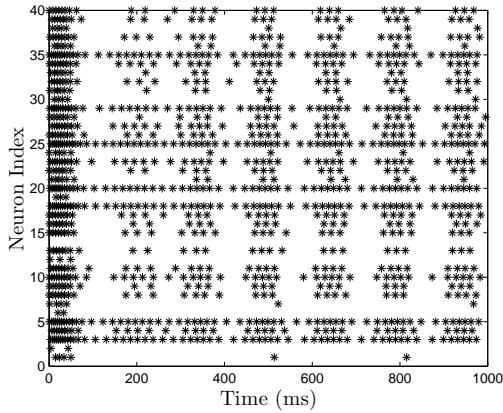


(b) Distribution of g_{syn} with $\mu_1 = 100$ nS, $\sigma_1 = 30$ nS, $\mu_2 = 300$ nS, $\sigma_2 = 50$ nS, $m = 0.4$

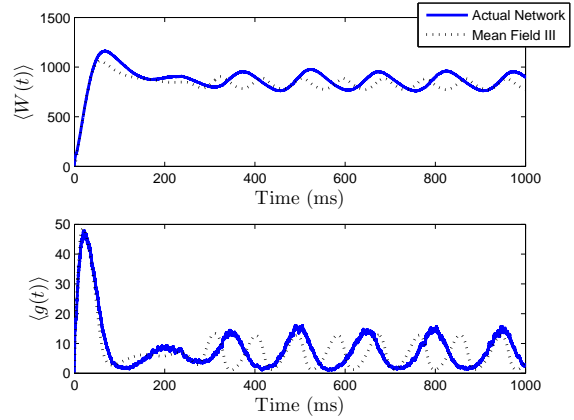


(c) Distribution of W_{jump} with $\mu_1 = 300$ pA, $\sigma_1 = 50$ pA, $\mu_2 = 75$ pA, $\sigma_2 = 20$ pA, $m = 0.6$

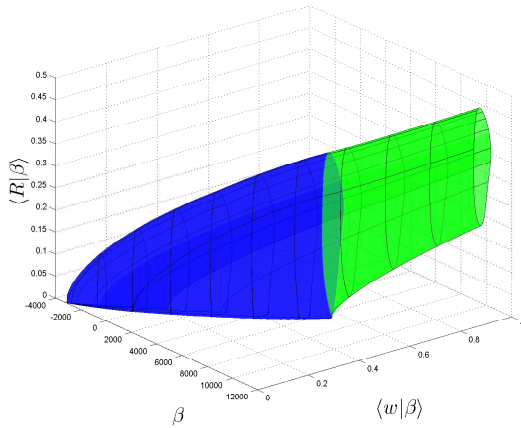
Figure 8: Bimodal distributions in I_{app} , g_{syn} , and W_{jump} lead to bimodal distributions in the firing rate. These bimodal parameter distributions are generated through distribution mixing of two normal subpopulations with standard deviations and means as indicated. See Appendix B for details. The distribution of the firing rate or the distribution of the parameter can be computed using MFIII if one knows the complementary distribution. See sections 3.2.2 and 3.2.3 for details. Curve descriptions are as given in Figure 7. Parameters, other than those indicated, can be found in Table 1. The calculations were carried out on a network of 1000 neurons.



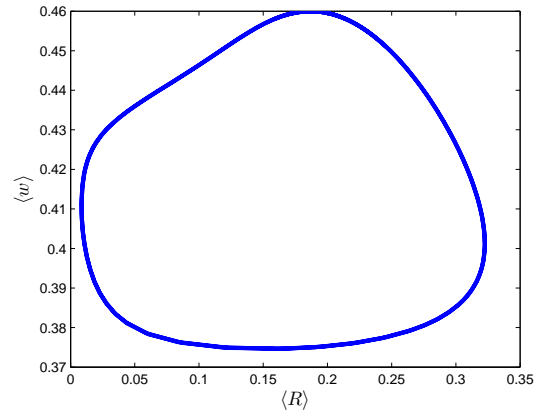
(a) Spike time raster plot of network behaviour



(b) Network and MFIII mean variables show oscillation

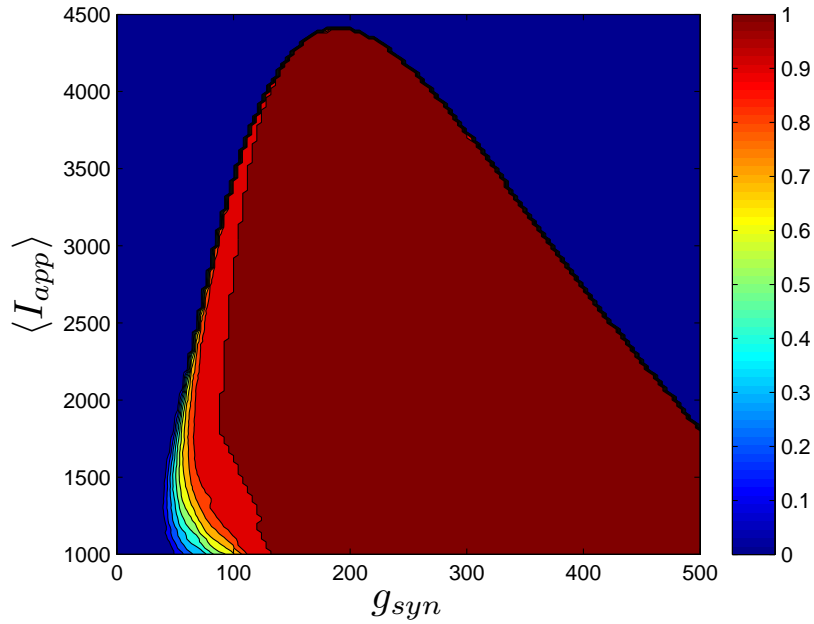


(c) MFIII limit cycle in conditional variables

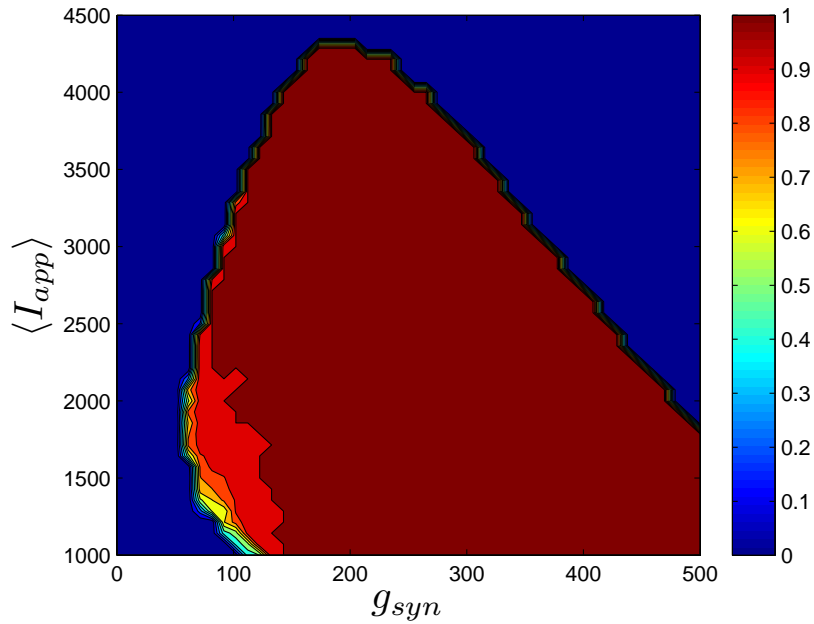


(d) MFIII limit cycle in mean variables

Figure 9: Visualizing a limit cycle in a heterogeneous network. Numerical simulation of MFIII and a network of 1000 neurons with heterogeneity in the applied current. Parameters are as given in Table 1 except $g_{syn} = 200$ nS, $\langle I_{app} \rangle = 1000$ pA and $\sigma_I = 4400$ pA. (a) Raster plot for 40 randomly selected neurons of the network. Some of the neurons are bursting, while others are tonically firing, albeit with an oscillatory firing rate. (b) In the mean variables, the steady state behaviour of both the network and MFIII is an oscillation. (c) As MFIII is a partial differential equation, the steady state “limit cycle” is actually a manifold of limit cycles, foliated by the heterogeneous parameter $\beta = I_{app}$. Part of the manifold has cycles with $\langle R|\beta \rangle = 0$ for an extended period of time (in blue), and the other part contains limit cycles that have $\langle R|\beta \rangle \neq 0$ during the entire oscillation. We can classify neurons with the parameter values in blue as bursting, and those in green as oscillatory firing. (d) Averaging the limit cycle in (c) with respect to β yields the mean limit cycle.

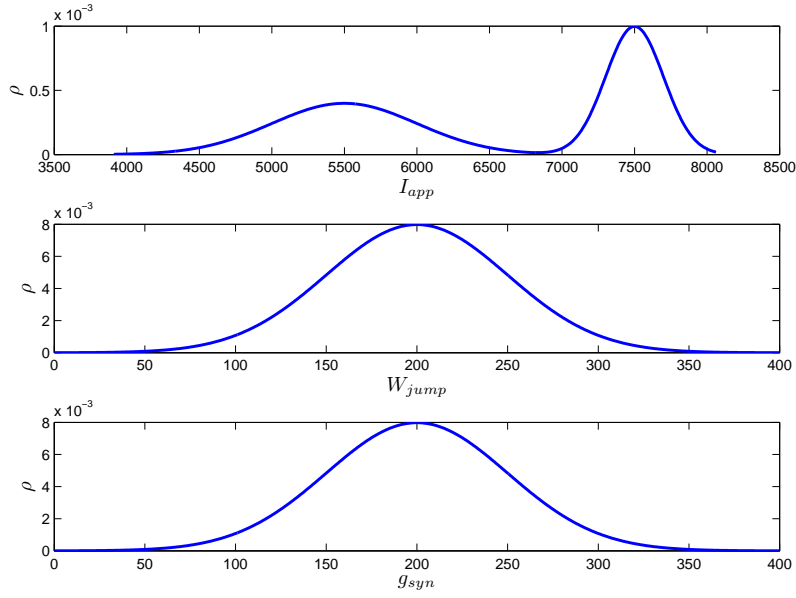


(a) MFIII, $\sigma_I = 500$ pA

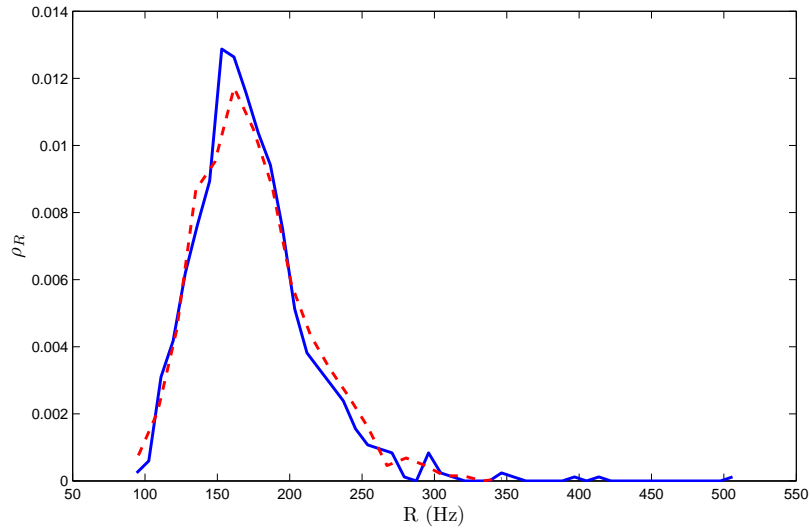


(b) Network, $\sigma_I = 500$ pA

Figure 10: The proportion of bursting neurons, p_{burst} for MFIII and an actual network. (a) Using the techniques outlined in the text, MFIII is used to compute the proportion of bursting neurons, p_{burst} at each point in a mesh over the parameter space. (b) Numerical simulations of a network of 500 neurons is used to compute the proportion of bursting neurons, p_{burst} . All the parameters for both the MFIII system, and the actual network are identical (see Table 1), except that MFIII is run over a finer mesh. The results using MFIII are both qualitatively and quantitatively accurate.

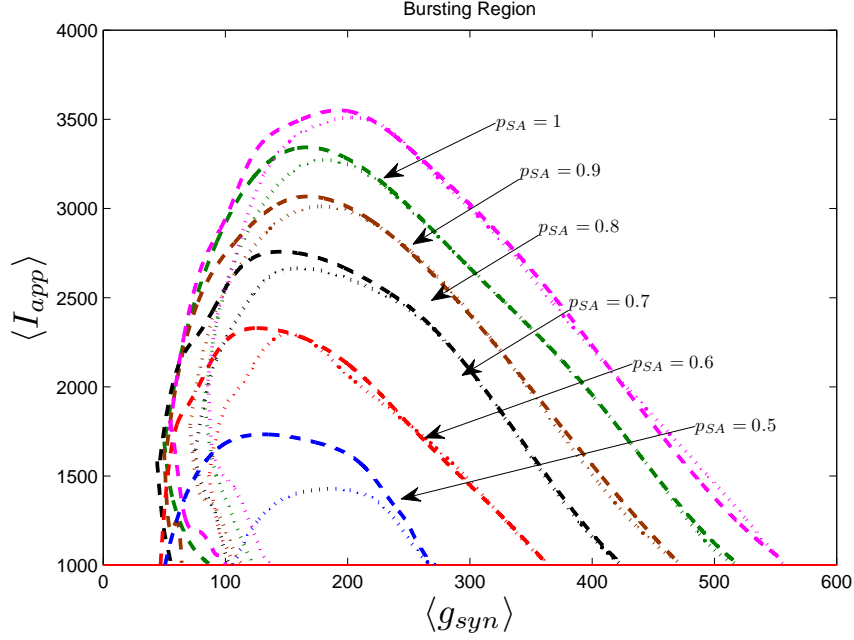


(a) Parameter distributions

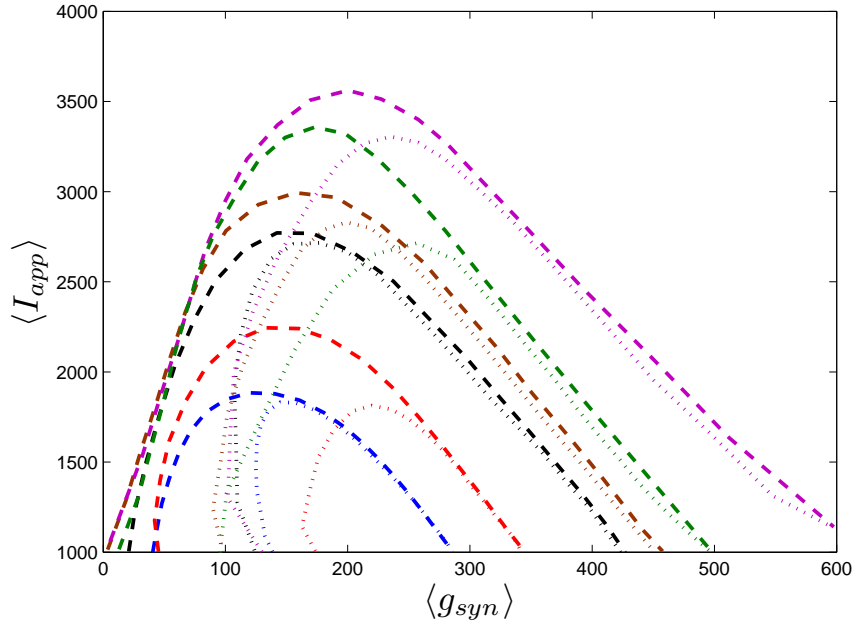


(b) Resulting firing rate distributions

Figure 11: A bimodal distribution in I_{app} together with unimodal distributions in g_{syn} and W_{jump} as shown in (a) yields a unimodal distribution in the firing rate (dashed curve in (b)). The mean-field equations give a good estimate of this distribution (solid curve in (b)). Simulations are for network of 1000 neurons. parameter given in Table 1 except I , g and W_{jump} . These are distributed with $\sigma_w = 50$, $\langle W_{jump} \rangle = 200$, $\sigma_g = 50$, $\langle g_{syn} \rangle = 200$, $m = 0.5$, $\langle I_{app,1} \rangle = 7500$, $\sigma_{I,1} = 200$, $\langle I_{app,2} \rangle = 5500$, $\sigma_{I,2} = 500$. Other combinations of bimodal and unimodal parameter distributions may yield bimodal firing rate distributions. Note that this is different than the situation shown in Figure 8, where a single bimodal source of heterogeneity yielded a bimodal firing rate distribution.



(a) Network bursting contours



(b) MFIII bursting contours

Figure 12: Case study: the proportion of bursting neurons in a network with both strongly adapting and weakly adapting neurons. Parameters are as in Table 1 except the I_{app} , g_{syn} , W_{jump} and τ_W which have bimodal distributions generated by distribution mixing with parameters given in Table 2. The parameter p_{SA} represents the proportion of strongly adapting neurons in the network (see equation (87)). The dashed line is the 0% bursting contour, while the dotted line is the 100% bursting contour. As shown in both the network (a) and MFIII (b), the bursting regions becomes significantly smaller when the proportion of strongly adapting neurons decreases. In all cases, the curves are smoother spline fits to the actual contours

Dimensional Parameters		Dimensionless Parameters	
C	250 pF		
k	2.5 nS/mV		
V_R	-65 mV		
V_T	$V_R + 40 - \frac{b}{k} = 41.7\text{mV}$	$\alpha = 1 + \frac{V_T}{ V_R }$	0.6215
V_{peak}	30 mV	$v_{peak} = 1 + \frac{V_{peak}}{ V_R }$	1.461
V_{reset}	-55 mV	$v_{reset} = 1 + \frac{V_{reset}}{ V_R }$	0.1538
W_{jump}	200 pA	$w_{jump} = \frac{W_{jump}}{k V_R ^2}$	0.0189
τ_W	200 ms	$a = \left(\frac{\tau_W k V_R }{C} \right)^{-1}$	0.0077
η	-1 nS	$b = \frac{\eta}{k V_R }$	-0.0062
I_{app}	1000 - 5000 pA	$I = \frac{I_{app}}{k V_R ^2}$	0.0776 - 0.3333
g_{syn}	0 - 600 nS	$g = \frac{g_{syn}}{k V_R }$	0 - 3.6923
τ_{syn}	4 ms	$\tau_s = \frac{\tau_{syn} k V_R }{C}$	2.6
s_{jump}	0.8		
N	1000		
σ_I	0 - 1000 pA		
σ_g	50 nS		
σ_d	50 pA		
m (mixing parameter)	0 - 1		

Table 1: The parameters and distribution variances used in this paper. These parameters apply unless otherwise indicated. Rheobase for the dimensional parameter values is $I_{rh} = 1000$ pA.

Parameter	Strongly Adapting	Weakly Adapting
$\langle g_{syn} \rangle$	0-600 nS	200 nS
$\langle \sigma_g \rangle$	$0.5 \langle g_{syn} \rangle$	50 nS
$\langle I_{app} \rangle$	1000-4000 pA	1200 pA
σ_I	500 pA	500 pA
$\langle W_{jump} \rangle$	200 pA	100 pA
σ_{W_j}	50 pA	20 pA
$\langle \tau_w \rangle$	200 ms	50 ms
σ_{τ_w}	50 ms	10 ms

Table 2: Table of parameters for the strongly and weakly adapting heterogeneous subpopulations